

Live Wire - A Low-Complexity Body Channel Communication System for Landmark Identification

*Original*

Live Wire - A Low-Complexity Body Channel Communication System for Landmark Identification / Crepaldi, M.; Barcellona, A.; Zini, G.; Ansaldo, A.; Motto Ros, P.; Sanginario, A.; Cuccu, C.; Demarchi, D.; Brayda, L.. - In: IEEE TRANSACTIONS ON EMERGING TOPICS IN COMPUTING. - ISSN 2168-6750. - ELETTRONICO. - 9:3(2021), pp. 1248-1264. [10.1109/TETC.2020.2996280]

*Availability:*

This version is available at: 11583/2858381 since: 2020-12-21T16:44:13Z

*Publisher:*

IEEE Computer Society

*Published*

DOI:10.1109/TETC.2020.2996280

*Terms of use:*

This article is made available under terms and conditions as specified in the corresponding bibliographic description in the repository

*Publisher copyright*

IEEE postprint/Author's Accepted Manuscript

©2021 IEEE. Personal use of this material is permitted. Permission from IEEE must be obtained for all other uses, in any current or future media, including reprinting/republishing this material for advertising or promotional purposes, creating new collecting works, for resale or lists, or reuse of any copyrighted component of this work in other works.

(Article begins on next page)

# Live Wire – A Low-Complexity Body Channel Communication System for Landmark Identification

Marco Crepaldi<sup>1</sup>, Alessandro Barcellona<sup>1</sup>, Giorgio Zini<sup>1</sup>, Alberto Ansaldo<sup>2</sup>, Paolo Motto Ros<sup>3</sup>, Alessandro Sanginario<sup>3</sup>, Claudia Cuccu<sup>3</sup>, Danilo Demarchi<sup>3</sup> and Luca Brayda<sup>4</sup>

**Abstract**— This paper presents a robust simplex Body Channel Communication (BCC) system aimed at providing an interactive infrastructure solution for visually impaired people. Compared to existing BCC solutions, it provides high versatility, wearability and installability in an environment in a low complexity hardware-software solution. It operates with a ground referred-transmitter (TX) and it is based on an asynchronous threshold receiver (RX) architecture. Synchronization, demodulation and packetizing and threshold control are completely software defined and implemented using MicroPython. The RX includes Bluetooth® (BT) radio connectivity and a cell-phone application provides push text-to-speech notifications to a smartphone. The hardware achieves a Packet Error Rate (PER) of  $\sim 0.1$  at 550 kHz pulse center frequency, Synchronized-On Off Keying (S-OOK) modulation and 1 kbps data rate, for an average current consumption of 44 mA.

**Index Terms**— Body Channel Communication, Interactive Infrastructure, MicroPython.

## I. INTRODUCTION

Body Channel Communication (BCC) can be interpreted as the exchanging of information through a movable, living and self-contained transmission medium, that is, the human body. The original and main application idea behind BCC is to enable the private information exchange among wearable nodes placed on the human body, optionally connected to another portable concentrator operating as a gateway for the cloud or simple internet infrastructure connections [1]–[3]. Recent research trends, however, show an increased interest in the exploitation of BCC systems to enable interactive infrastructure communication [4]–[6]. This human-to-environment extension has led to the design of systems with diverse configurations in terms of electrodes placement both on- and off-body [7], [8]. Thanks to BCC, space can be interactively explored as a person must touch the surrounding objects to gather information.

The above aspect is paramount in applications for visually impaired people, who regularly seek for information with an active limb motion. This is a substantially different way of interacting with the environment compared to RFID

[9], Beacon [10], and Impulse Radio Ultra-Wide Band (IR-UWB) [11] because these systems trigger interactions with humans regardless of physical haptic contact with the external world. Previous works introduced the concept of Capacitive Near-Field Communication (CapNFC) where capacitive communication can be used to enable ubiquitous interaction with objects in short-range spatial contexts [12]. However, CapNFC has been developed so that the user human body takes part in the transmission but it is not the final information recipient. Our research targets the implementation of a low-cost and low-complexity BCC system suitable for such human-to-environment extension, with awareness on the current consumer market trends (see, e.g., [13]) that include voice-assistance and integration in smart homes. Our solution, *Live Wire* (see preliminary results in [14]), is a kHz-range threshold-based impulse-radio non-coherent system (simplex TX-to-RX link) that solves the problem of co-locating haptic interaction with an object and the reception of digital information. It is intended to be implemented using low cost components, full programmability and the highest *installability* in the environment. *Live Wire* takes advantage of the low-frequency electric field approximation of the human body (quasi-static near-field) and at the same time of the ground connection of the TX. Owing to its features, the TX can be installed on any conductive object in the environment with ideally any possible shape, and it operates with a very low current. Being the TX directly connected to the reference voltage (ground), when the TX is touched, the human body acts as a wire by providing the signal at almost the same level throughout the body, therefore enabling both a high-impedance pick-up and a constant Signal-to-Noise Ratio (SNR), almost independent from the RX positioning. Moreover, the RX does not need to be in contact with the skin.

To counterbalance the human body electrical features variability, BCC devices encompass the use of tunable inductors to implement resonance w.r.t. coupling capacitance [15], [16]. In these cases an SNR enhancement is necessary as in capacitive BCC one out of two electrodes (both for TX and RX) are floating and the other is in contact with the skin and positioned vertically or horizontally w.r.t. the human body [17]. While this requirement normally impacts on system complexity, in *Live Wire* given the enforced low-impedance path to ground at the TX, the SNR remains constant throughout the body. Adaptativity, instead, is here translated into a front-end dynamic threshold adjustment to counterbalance environmental interference. Consequently an automatic gain control unit (AGC), see e.g. [18], is not required.

M. Crepaldi, A. Barcellona and G. Zini are with 1) the Istituto Italiano di Tecnologia (IIT) – Electronic Design Laboratory (EDL), Via Melon 83, 16152 Genova (GE), Italy, e-mail: marco.crepaldi@iit.it. A. Ansaldo is with 2) the Istituto Italiano di Tecnologia (IIT) – Graphene Labs, Via Morego 30, 16163 Genova (GE), Italy. P. Motto Ros, A. Sanginario, C. Cuccu and D. Demarchi are with 3) the Politecnico di Torino, Department of Electronics and Telecommunications, C.so. Castelfidardo 39, 10129 Torino (TO), Italy. L. Brayda is with 4) the Istituto Italiano di Tecnologia (IIT) – Robotics Brain and Cognitive Sciences (RBCS), Via Melon 83, 16152 Genova (GE), Italy.

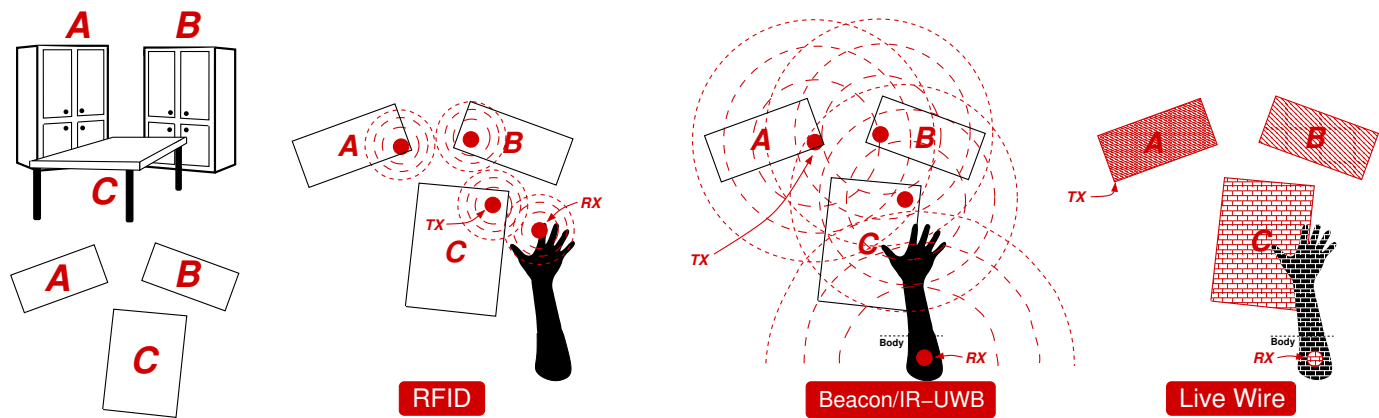


Fig. 1. Comparison between the RFID, Bluetooth® low energy Beacon/IR-UWB and *Live Wire* (BCC) technology.

87 *Live Wire* requires just a microcontroller I/O pin to drive  
 88 the TX signal and a low-complexity front-end detector at  
 89 the RX based on very limited number of external active  
 90 components. Moreover, it is fully implemented using MicroPy-  
 91 thon ( $\mu$ Py), an open source and easily extensible high-level  
 92 programming language, increasingly used in real-time system  
 93 development (see [19] and research in [20]) and considered  
 94 as an interesting alternative to empower embedded systems  
 95 [21]. Our contribution regards i) an innovative application  
 96 to increase quality of life of visually impaired people, ii)  
 97 an HW/SW architecture for landmarks exploration in smart  
 98 environments, iii) an associated threshold control algorithm,  
 99 iv) a working prototype including an experimental validation  
 100 of the system. The paper is organized as follows: Sec. II  
 101 details the application domain, Sec. III discusses the system  
 102 architecture, and Sec. IV–V detail TX and RX prototype, the  
 103 RX threshold adjustment algorithm, the RX internal firmware.  
 104 Sec. VI presents detailed performance measurement results  
 105 and functional validation obtained by installing the TX in  
 106 different furniture, simply grounded through a USB port, and  
 107 concludes with a state-of-the art comparison.

## 108 II. MOTIVATION AND APPLICABILITY

109 The application of the *Live Wire* technology is the identi-  
 110 fication of landmarks for visually impaired persons. *Live Wire*,  
 111 unlike current approaches such as RFID and BT low-energy  
 112 Beacon, is designed to allow a person without vision to seam-  
 113 lessly obtain digital information from common objects only  
 114 by touching any part of them. The identification of landmarks  
 115 is crucial because it is at the foundation of blind persons  
 116 orientation and mobility strategies [22]. Without correctly  
 117 identifying landmarks, navigation for blind persons is either  
 118 too difficult or it must entirely rely on guides or technological  
 119 aids, thus preventing the learning from the environment and  
 120 implying relevant safety concerns. The literature is populated  
 121 with Electronic Travel Aids (ETA) that very often increase  
 122 the cognitive load of the landmark identification process,  
 123 something known as the “masking phenomenon” [23]. Even if  
 124 there is a large literature of indoor navigation systems (see [24]  
 125 for a review), most studies focus on assisted navigation and  
 126 only a few works consider that navigation is already a well-

trained process in blind persons, but landmark identification  
 is not. Usually, blind persons identify large objects (furniture,  
 home appliances) by means of Braille tags [25]. Due to their  
 very small size compared with the object surface, they have  
 to be found by an extensive tactile exploration, thus resulting  
 uncomfortable, they cannot contain extensive information and  
 cannot be tailored to user needs.

Fig. 1 compares three technological solutions to this prob-  
 lem, i.e., RFID, Beacon/IR-UWB and *Live Wire*. Here, three  
 possible objects, i.e., closets A and B, and desktop C have to be  
 unambiguously identified by the arm of a blind person. RFID  
 has the advantage of deploying passive transmitters on any  
 object, but it is known to have a limited radiation pattern. This  
 forces the end-user to wear the transceiver in distal parts of the  
 body (e.g. the closest to the hand) and to search for the RFID  
 tag as in the Braille tag case, but without the advantage of  
 explicit tactile feedback (RFID tags are not necessarily in re-  
 lief). Beacons provide extended range, but crosstalk can make  
 object pinpointing complicated. Importantly, with beacons the  
 ecologic process of landmark identification, usually achieved  
 with active haptic exploration, is completely decoupled from  
 reception of data from the beacons. However, unlike RFID,  
 Beacon allows wearing the receiver in any body part. *Live Wire*,  
 instead, collects the advantages of their predecessors,  
 without being limited by their drawbacks: *Live Wire* sends  
 information from objects *only* if they are touched; it has the  
 advantage of extending the range of information to the whole  
 surface of an object without the disadvantage of crosstalk.

IR-UWB, similarly to Beacon, can enable location but more  
 precisely. However, its performance strongly depends on Line-  
 of-Sight (LOS) or Non-Line-Of-Sight (NLOS) conditions.  
 Even in the best accuracy condition of  $\pm 10$  cm in LOS [11]  
 accuracy is not sufficient, and the transceiver must be in close  
 proximity with the object to be approached (with anchor nodes  
 disseminated in the environment). A key point of *Live Wire*,  
 instead, is that digital information is confined to the same  
 haptic enclosure, therefore avoiding confusion between objects  
 and preventing false alarms: digital information is co-located  
 with haptic exploration. Moreover, the *Live Wire* RX can  
 be worn anywhere on the body, e.g. inside cloths, therefore  
 allowing interaction with hands, arms, legs. We expect that

blind persons using *Live Wire* would find natural to learn landmarks, since the process of identification is triggered by haptic exploration and enriched, for example, with audio information (e.g. “this is the closet with winter clothes” or “this shelf hosts biscuits and sweets” or “the table you are touching is at the center of the room”).

### III. LIVE WIRE BCC

#### A. High-Level Constraints

In commercial solutions such as BodyCom [26] transmission is based on a resonant LC load and base station (fixed node) and mobile device (wearable node) is initiated thanks to a capacitive touch detection on a pad electrode. The center frequency utilized for bidirectional communication is 125 kHz, that exploits the high permittivity of the human body which permits low-complexity transmission in the 60 kHz–10 MHz frequency range. However, due to capacitive/proximity detection and LC resonance, the pad needs to be carefully designed, which is totally in contrast with our application domain in which the user must have the freedom to touch any (metallic) part of the object in the infrastructure.

For applications involving able-bodied persons, the typical latency of human perception is 150 ms [27], while in other specific BCC implementation latency is considered in the range 10 – 250 ms [28]. In general, these latency constraints can be applied to visually impaired people as well, as for these subjects the only difference is in the sensory modality with which information is received. However, the above bounds are valid in a real-time application in which latency is considered as a direct player in a closed perception/actuation loop (for instance drag and drop actions in touch-screens). In our case, in which the environment transmits information to the user in one direction and touch involves a more complex activity compared to drag-and-drop or click on a touchscreen, a latency even in the order of seconds can be tolerated [29]. To enable environmental exploration, it is essential that received data is transmitted to a more complex portable device so that it can be processed to be converted into other kinds of feedback, e.g., auditory, haptic (vibration), or even, depending on the environment extension and on the application, logged on the Cloud. Therefore, to maximize connectivity, a wearable node needs to include a wireless transceiver normally present in consumer smartphone or tablets. Compared to [4], BT connectivity is increasingly preferred instead of Wi-Fi to reduce power consumption. In our context, BT can be effectively used thanks to the low data rate requirements of the application specified in [14]. At the same time, at a fixed node side the presence of wireless connectivity is still fundamental, but to enable landmark configurability or dynamic information transmission (landmark data can change over time).

#### B. Architecture

Fig. 2 shows a conceptual scheme of our *Live Wire* BCC. It comprises a TX that must be connected through a low-impedance path to ground. The TX drives a high impedance load, which is the human body, that in standard operating conditions is floating. A wearable RX, that is capacitively

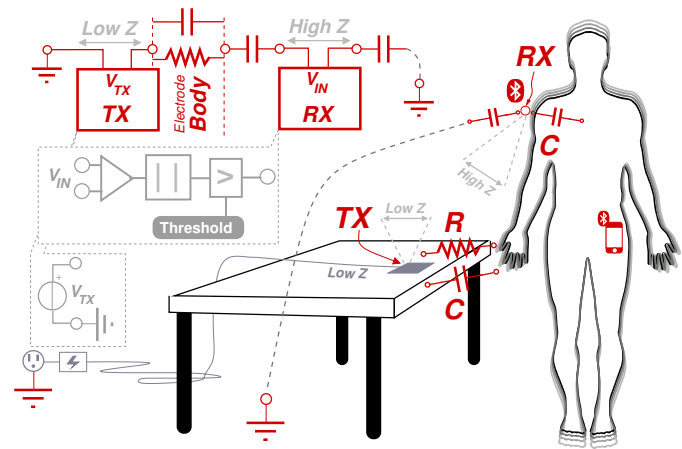


Fig. 2. Block scheme of the *Live Wire* BCC system.

coupled through the body and to the return path to ground, detects the signal through a high impedance input stage. The current required to operate the system, similarly to other capacitive BCC systems, is extremely limited by construction, accounting few tens of nA only. The TX can be implemented using a simple microcontroller that drives the TX electrode that overall is loaded capacitively.

The RX is in charge of amplifying, demodulating and synchronizing the incoming modulated signal, which has a sub-MHz center frequency. In our implementation a 550 kHz center frequency, corresponding to the highest speed achieved using our  $\mu$ Python rapid prototyping software solution, is used. This frequency falls in the interval used in commercial solutions and permit low-complexity transmission [26]. Thanks to its inherent non-coherent and non-linear nature, the RX is able to detect distorted signals, therefore enabling constraints to be relaxed for the TX as well. Indeed, a perfectly sinusoidal output is not strictly required, and modulation synthesis can be done by square waves, enabling the use of any digital General Purpose Input/Output (GPIO) in the TX microcontroller, that typically operates in a 3–5 V range. The full swing signal drives directly the human body, to which the RX couples. It exploits a square electrode (in principle non in contact with the skin) and the PCB ground to create a capacitive coupling.

The tens of mV signal coupled at the RX input can be then amplified using a low-complexity front-end, rectified, thresholded and then sampled (at baseband speed, i.e., symbol rate) using, similarly, a GPIO generic input of a microcontroller. The processor can implement, in a software-defined fashion, both demodulation and synchronization. Unlike typical state-of-the-art solutions, in which RX are based on e.g., down-conversion [4], Orthogonal Frequency Domain Multiplexing (OFDM) [18], wideband signaling [30], super-regeneration [31] or injection locking [32], similarly to [7], the *Live Wire* RX rectifies the complete incoming wave, therefore including both signal and other potential disturbances that may be coupled through the human body. This assumption implies a lower complexity hardware compared to standard solutions, while not significantly impacting on performance, as will be further demonstrated in Sec. VI.



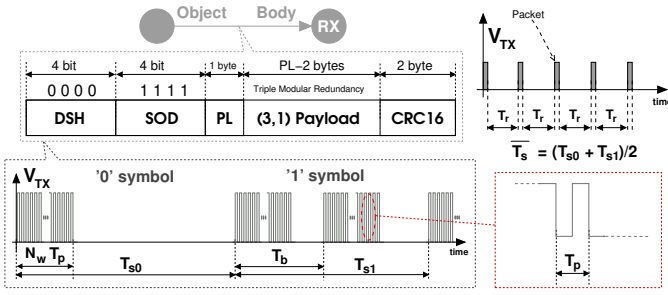


Fig. 3. S-OOK modulation, here asymmetric with different symbol duration for '0' and '1', with packet format and periodic TX access.

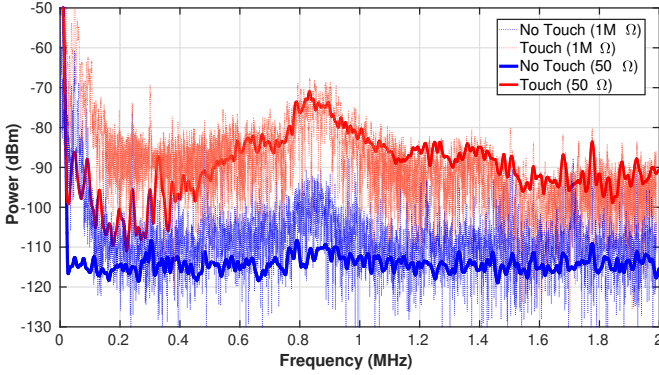


Fig. 4. Measured input power from the human body using a  $3 \times 2$  cm electrode connected to a  $50 \Omega$  input RSA3408B real-time spectrum analyzer (resolution bandwidth 10 kHz), and to a DSO9404A (Fast Fourier Transform, resolution bandwidth 625 Hz, input impedance 1 M $\Omega$ ). The background levels corresponding to a no touch condition, are depicted for both cases.

### C. Modulation and Signaling

In terms of physical-layer modulation, BCC can encompass very different modulation techniques, ranging Quadrature-Phase Shift Keying (Q-PSK) [28], Bi-Phase Shift Keying (B-PSK) or On-Off Keying (OOK) [33]. In this work we have selected a self-synchronized version of OOK [an on/off digital variant of Amplitude Shift Keying (ASK)] thanks to its advantages in terms of power consumption (i.e., transmitter circuit active only when a '1' symbol is transmitted). OOK modulation is indeed a typical choice in capacitive BCC [4]. ASK, *inter alia*, is more suitable for short-range implant devices and telemetry systems with respect Frequency Shift Keying (FSK) and PSK, thanks to its simple associated hardware implementation and resulting size [34].

Fig. 3 shows the *Live Wire* Synchronized-On Off Keying (S-OOK) modulation format. The pulses center frequency is  $1/T_p$ . Each symbol comprises a square wave of  $N_w$  periods (overall lasting  $N_w T_p$ ), sync-to-sync pulse delays  $T_{s0}$  and  $T_{s1}$  (average symbol timing  $\bar{T}_s$ ) and sync-to-data delay  $T_b$ .  $T_r$  is the packet repetition delay. Observe that, in S-OOK, it is not required that symbol duration is equal for both a '0' and '1' symbol, while it is necessary that synch-to-data delay is controlled [35], even with low accuracy. At implementation-level this enables relaxation in terms of signal generation timing, thus tolerating mismatch between '0' and '1' symbol duration. This is beneficial especially when modulation and demodulation are implemented at software-level, hence relaxing constraints on

context switching delay between processes.

Packets comprise a Data Synchronization Header (DSH), a Start-Of-frame Delimiter (SOD), a Packet Length field (PL), a Payload and a Cyclic Redundancy Check (CRC). To ensure a reliable data transmission during landmark identification, indeed, the transmission needs to consider both a CRC for each packet and an Error Correction Code (ECC) so that symbols can be recovered also in case of bit flips due to noise and disturbance introduced by the body channel. *Live Wire* uses a CRC-16-CCITT standard CRC which has been extensively used e.g., for Bluetooth® and XMODEM. This CRC has been selected because packet length can vary, for our application from few to up to dozens of bytes. The selection of ECC codes used, at least in Wireless Sensor Networks (WSN), varies based on an implementation power consumption and performance trade-off [36]. *Live Wire* is based on a relatively high SNR transmission using very low power. Communication needs to be established only if the transmitter is in contact with the human body. Therefore, we have selected a very low complexity (3,1) Hamming code (triple modular redundancy) towards the energy efficiency side. All packet parameters are defined at software-level and can be modified according to the application. In this implementation both DSH and SOD have a fixed length of 4 bit. PL has a length of 1 byte and the payload length is variable between 0 and 255 byte. The CRC-16-CCITT length, computed on the (3,1) encoded payload, is 2 byte. In terms of channel access, the TX anchor, that receives an AC network-derived power supply and a ground reference through the USB port, continuously transmits packets using a periodical access with a delay of  $T_r$  between contiguous packets.

In *Live Wire* system latency can be specifically designed based on symbol timing, packets repetition frequency and length. In general, packet timing must satisfy the inequality  $\bar{T}_s 8N_{\text{bytes}} + T_r < \Delta_L$ , where  $\Delta_L$  is the posed system latency and  $N_{\text{bytes}}$  is the number of bytes in the packet. Observe that if for a 2 bytes payload, including for instance one byte that codifies the landmark and another that carries status information,  $T_r = 50$  ms and  $\bar{T}_s = 909 \mu\text{s}$ , by considering coding we obtain  $122 \text{ ms} < \Delta_L$ , which still satisfies the latency of human perception considered in literature.

### D. Threshold Control

Fig. 4 shows the effect of touching a copper electrode (wire length 13 cm and connected to a female SMA connector) referred to the AC power distribution ground, using a  $50 \Omega$  input spectrum analyzer and a  $1 \text{ M}\Omega$  input impedance oscilloscope in a laboratory environment. When the TX electrode is in contact with the human body, therefore it is shunted to a low-impedance path to ground, the body captures interference sources in the environment and operates as a wire (or an antenna below 200 MHz thanks to its high dielectric constant [37]). In a 500 kHz bandwidth (center frequency 500 kHz), on a  $1 \text{ M}\Omega$  impedance, an overall average power of -44 dBm is available at the receiver input, that corresponds to an average input voltage  $V_{RX}$  of  $\sim 180$  mV (computed from  $P_{IN} = \frac{V_{RX}^2}{R}$ , where  $P_{IN}$  is power and  $R = 1 \text{ M}\Omega$ ). In case of no touch, the

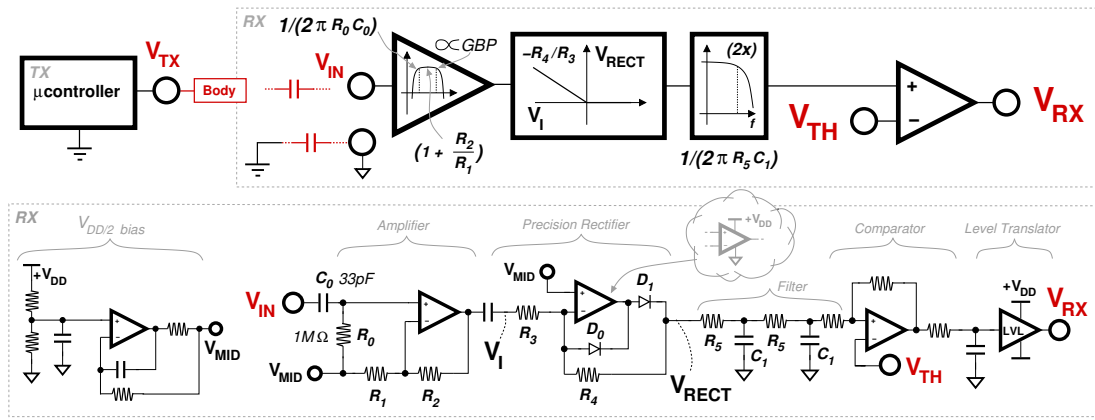


Fig. 5. *Live Wire* block scheme and RX front-end schematic.

346 average input power is on the order of  $-68$  dBm, which is  
 347 translated into a  $V_{RX}$  of  $\sim 13$  mV.

348 These average figures of merit are an indication of the  
 349 disturbance power level that may be captured by the receiver,  
 350 and confirm that interference is captured by our high input  
 351 impedance front-end and most important, disturbance is dyn-  
 352 amical and highly depending on the surrounding environment  
 353 including existing wireless networks [37]. For this reasons,  
 354 the *Live Wire* RX shall be able to adjust the threshold used  
 355 to demodulate data. Threshold control does not represent for  
 356 our system a significant complexity point: it can be achieved,  
 357 as will be detailed next, using a simple algorithm that starts  
 358 from a minimum threshold level and increases it linearly  
 359 until no noise or interference triggers are present. With an  
 360 energy detection front-end, such linear threshold adjustment  
 361 is an effective solution in cognitive radios [38]. These radios,  
 362 dynamically configure front-end to achieve the best perfor-  
 363 mance in presence of interference and prevent congestion. In  
 364 our context the problem to be solved is similar, because the  
 365 receiver does not need to be jammed in presence of large  
 366 interference.

#### IV. HARDWARE DESIGN

##### A. Block Scheme and RX Front-end

369 Fig. 5 shows a block scheme of our *Live Wire* prototype,  
 370 with a detail on the schematic of the RX front-end. As  
 371 previously introduced, the transmitter is based on a low-  
 372 impedance GPIO output of a  $\sim 3$  V powered microcontroller,  
 373 that can be software programmed. The RX front-end comprises  
 374 an amplifier, a rectifier a low-pass filter and a continuous  
 375 time threshold comparator. The incoming BCC signaling wave  
 376 is amplified using a high gain-bandwidth product single rail  
 377 AD8028A OpAmp, to enable the reception of pulses with  
 378 center frequency in the range  $5$  kHz– $1$  MHz, thus providing  
 379 a larger degree of freedom for the development. Moreover,  
 380 to minimize the number of energy sources, the amplification  
 381 front-end has a single power supply. Non-coherent detection  
 382 is provided by the Precision Rectifier, whose output  
 383 is filtered and thresholded using the comparator that has a  
 384 positive feedback to introduce hysteresis, implemented with  
 385 the same OpAmp. The reference voltage  $V_{MID}$  is derived

386 from the  $2.83$  V voltage supply  $V_{DD}$ , divided by two by a  
 387 voltage divider (left) and buffered using an OpAmp. The first  
 388 Amplifier stage does not include capacitors to fully exploit  
 389 the high Gain-Bandwidth Product (GBP) of the OpAmp, and  
 390 has a nominal gain of  $30$  dB.

391 The system implements AC mains supply ( $50$  Hz nominal  
 392 frequency in Europe) noise filtering using the high pass  
 393 filter made of  $C_0$  and  $R_0$ , nominally  $33$  pF and  $1$  M $\Omega$ , which  
 394 corresponds to a  $-3$  dB cut-off frequency of  $4.8$  kHz. As the  
 395 AD8028A provides a dedicated stand-by signal, the front-end  
 396 can be now turned off by the microcontroller in idle state  
 397 to save power (signal not shown for the sake of brevity).  
 398 The rectifier, that provides phase inversion for negative signal  
 399 values, has a nominal gain of  $47$ . The Schottky diodes  $D_0$   
 400 and  $D_1$  in the rectifier are CFSH-4. After rectification the  
 401 signal is low-pass filtered using a two poles low-pass filter  
 402 implemented with  $R_5$  and  $C_1$ , providing a cut-off frequency  
 403 of  $125$  kHz. Nominally,  $R_0=1$  M $\Omega$ ,  $R_1=10$  k $\Omega$ ,  $R_2=330$  k $\Omega$ ,  
 404  $C_0=33$  pF,  $C_1=47$  pF,  $R_3=4.7$  k $\Omega$ ,  $R_4=220$  k $\Omega$  and  $R_5=27$  k $\Omega$ .

##### B. TX and RX PCB Modules

405 Fig. 6 shows the block scheme of both wearable and anchor  
 406 nodes, i.e., RX and TX, respectively. As transmission is  
 407 based on high-impedance signaling, TX symbols generation  
 408 is simply implemented using a GPIO output of a microcon-  
 409 troller running digital  $0-V_{DD}$  transitions. This pin, is directly  
 410 connected though a decoupling capacitor to a metallic pick-  
 411 up, that, in turn, can be fixed to an anchor object. By touch-  
 412 ing the metallic element, as previously discussed, the human  
 413 body turns into a “wire”, allowing the RX to capture TX sym-  
 414 bols thanks to an high input impedance of  $\sim 1$  M $\Omega$ . Both TX  
 415 and RX devices comprise an L-series STM32L486 MPU,  
 416 running  $\mu$ Py version 1.9.1, that we have ported (and patched  
 417 to enable the use on-chip DAC) from the officially supported  
 418 F-series STM32 port [19]. The modules comprise the Bluegiga  
 419 BGM123A module that communicates with the  $\mu$ controller  
 420 that transmits commands and receives BT events through a  
 421 Universal Asynchronous Receive and Transmit UART port con-  
 422 figured with enabled flow control. Both devices provide  $\mu$ USB  
 423 connectors to enable power supply/battery recharge using a  
 424 BQ24230 and TPS78001, LDO and battery charger, respec-  
 425

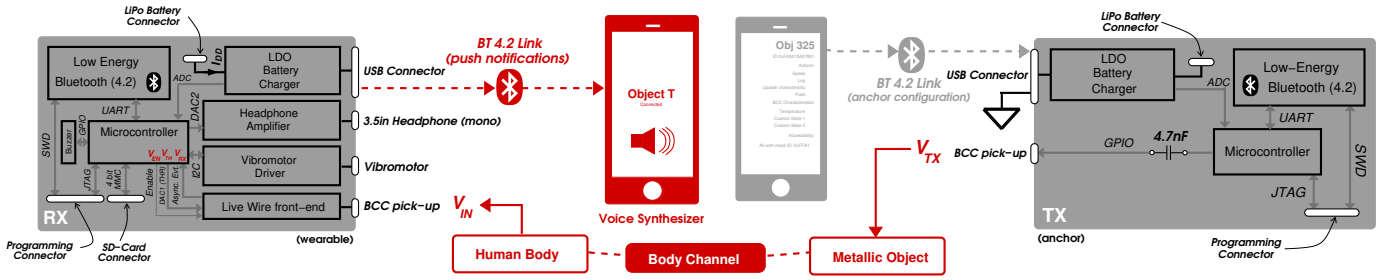


Fig. 6.  $\mu$ Python-based RX (wearable node) and TX (anchor node) block scheme comprising wireless interconnection with an external smartphone.

tively (3.7 V, 250 mAh nominal capacity). The power supply is set to 2.83 V, the minimum voltage to enable all components operation, maintaining a lower power consumption compared to the standard 3.3 V supply. This way, as battery voltage decreases, the available charge can be exploited as much as possible and increase device lifetime. For the TX (which, in any case, needs to be connected to the infrastructure) the LiPo battery operates as a back-up in case the voltage supply provided by the  $\mu$ USB connector is interrupted. The TX series decoupling capacitor has a nominal value of 4.7 nF. Observe that such capacitor has an impedance at 550 kHz as low as  $\sim 62 \Omega$ , therefore not significantly impacting on the conceptual transmission scheme previously described.

The analog front-end, has a threshold  $V_{TH}$  controlled by a first STM32 DAC (DAC1 in figure). The asynchronous events (Asynch. Evt.) received from the RX front-end are transferred to a general purpose digital I/O of the  $\mu$ controller. The RX module comprises both a DRV2605 vibromotor driver connected to the microprocessor through an I2C interface, and a TS4211ST mono headphone amplifier (with the corresponding 3.5 in connector) directly driven by a second STM32 DAC [DAC2 in Fig. 6]. Both TX and RX systems can be programmed through a dedicated connector and a full-custom programming board (not shown) using a JTAG and a SWD interface, for the MPU and the BT 4.2 chip, respectively. The RX  $\mu$ controller is connected through a Quad-SPI port (4bit MMC interface) using an SMD connector to an external SD-card, that is powered using the 2.83 V main voltage supply. Finally, the RX board comprises a buzzer connected to the MPU using a dedicated GPIO.

The BT 4.2 link, at the RX side, enables push notifications to a portable device. At the TX side, BT can be used to update configuration or update anchor status data with wearable nodes information. The TX BT transceiver can be also utilized jointly with the BCC link to implement a full duplex communication with the anchor node. A portable device, such as a smartphone, upon reception of an event from the anchor through the BCC PHY link, can then establish a BT connection with the TX and exchange information.

## V. FIRMWARE DESIGN

### A. TX

The BCC signaling waveform is digitally generated by a TX GPIO using the  $\mu$ Py Viper code emitter [39]. In our implementation,  $T_r$  can vary. For our error-rate tests we kept

$T_r = 250$  ms for ease of testability, while for other functional tests we kept  $T_r = 50$  ms.  $T_{s0}$  is  $848 \mu s$ ,  $T_{s1}$  is  $970 \mu s$ ,  $T_b$  is  $520 \mu s$ , pulses center frequency is 550 kHz and  $N_w = 96$ . The pulse parameters have been selected based on extensive functional tests in the environments of Fig. 17(a).

### B. RX Synchronization and Demodulation

Fig. 7 shows a simplified flow chart of the RX firmware. The signal detection loop inherently includes a Clear Channel Assessment (CCA) based on a rectifier (similar to an energy detector [40]), which is used to establish the absence of a transmitted signal, and in turn run threshold control and adjust the front-end selectivity to minimize error-rate and avoid RX jamming. The *Live Wire* TX electrode (or the associated object), that repeatedly transmits packets, can be touched anytime and in general asynchronously by the user, also during the transmittal of a packet, which opens the way of a series of cases that the receiver needs to handle to ensure service availability. During the main loop start-up (left), after peripherals initialization (including GPIO, front-end, headphone driver, vibromotor) and internal variables reset, the system updates the BT chip status, to make sure the radio is set in advertising mode, hence discoverable by other devices. Demodulation and synchronization is based on a continuous polling on  $V_{RX}$  based on an iteration counter `num`, a symbol number counter `lp`, a timeout counter `num_to`, a last symbol detection counter `timenow` and a set of status flags to identify the various PHY packet fields. The idea is to continuously check for a GPIO transition, and if detected, decode a symbol (and check the corresponding delayed data bit through another GPIO read, not shown in the flow chart) and update a vector of received symbols `RX_SYM_VECT` that in turn needs to be tracked at every iteration. The internal logic routine `Decode packet (lp)` keeps track of the progressive reception of the symbols and returns continuation, valid and invalid conditions depending on the content of `RX_SYM_VECT`. If a packet is correctly received (the CRC is correct), the received payload is sent to the BT (Write BT Characteristic) that, if connected, transmits the data (notification) to the connected device. After transmission the system plays a wave file or alternatively buzzes a sound and restarts from threshold adjustment. In case of an invalid packet (incorrect CRC or DSH/SOD) the status variables are simply reset to restart from `Adjust THR`, the routine that controls threshold that will be detailed next. This corresponds to the condition `THR Error`, i.e., threshold control is re-initiated because the packet reception sequence has been interrupted.



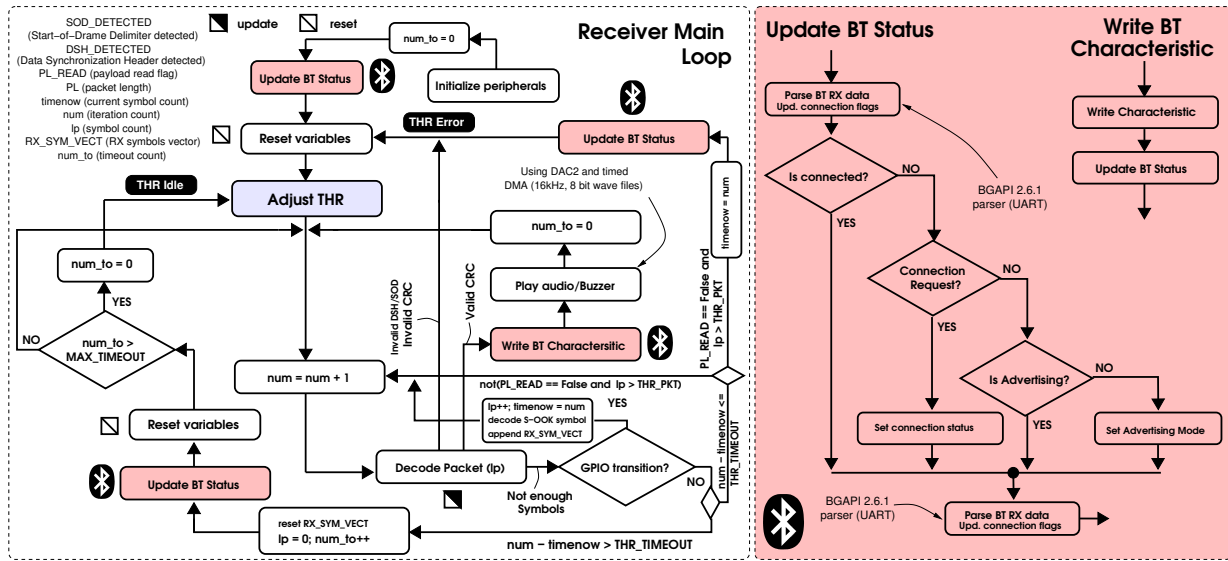


Fig. 7. (left) RX main infinite loop controlling both PHY layer, BT communication and module I/O peripherals, (right) detail on the BT status update routine.

### Algorithm 1: Threshold Control

**Result:** DAC output  $V_{TH}$  for the RX front-end.

$THR = THR_{min}$ ;

$V_{TH} = V_{DD}THR/255$ ;

$\tau = 0$ ;

$t = 0$ ;

**while**  $\tau \leq T_{timeout}$  **do**

**while**  $t \leq T_{min}$  **do**

$\tau = 0$ ;

**if**  $V_{RX} = '1'$  **then**

$t = 0$ ;

$THR = THR + 1$ ;

$V_{TH} = V_{DD}THR/255$ ;

      Wait for  $\Delta t_{on}$ ;

**else**

$t = t + \Delta t$ ;

**end**

    Wait for  $\Delta t$ ;

**end**

**if**  $V_{RX} = '1'$  **then**

$t = 0$ ;

$THR = THR + 1$ ;

$V_{TH} = V_{DD}THR/255$ ;

    Wait for  $\Delta t_{on}$ ;

**else**

$\tau = \tau + \Delta t$ ;

**end**

  Wait for  $\Delta t$ ;

**end**

Update  $V_{THR}$  with  $THR$  (fixed length  $M$ );

$THR = \overline{V_{THR}}$ ;

$V_{TH} = V_{DD}THR/255$ ;

To ensure a correct reception this simple mechanism is not enough as it may happen that due to insufficient signal drive symbols are not received correctly. To overcome this problem two restart conditions are given using two thresholds, a symbol duration timeout ( $THR\_TIMEOUT$ ) and a packet length threshold ( $THR\_PKT$ ). The first threshold is used to detect a timeout after a symbol is received: as the transmitted symbols have a fixed  $T_{s0} + T_b$ , waiting more than the expected symbol duration is an indication of reception of an end of a corrupted packet. The system can then increase the timeout counter  $num\_to$  and reset the received symbol counter  $lp$  with the corresponding vector, variables and restart without threshold adjustment because the touch event started during the transmission of a packet, therefore RX shall immediately capture the next transmitted packet. If packet reception is not completed successfully after a number of trials  $MAX\_TIMEOUT$ , the system restarts from threshold adjustment, even if the subject is still touching the TX electrode. Observe that linear threshold adjustment, notwithstanding being an heuristic approach, can operate also in presence of a busy channel [38]. In the diagram, this new threshold adjustment corresponds to the condition  $THR\_Idle$ . The use of the second threshold  $THR\_PKT$  is combined with a condition on the ongoing payload demodulation, that is  $(PL\_READ == False \text{ and } lp > THR\_PKT)$ , where  $PL\_READ$  is a flag that indicates that payload is being read. If the system status after  $THR\_PKT$  symbols is not reading the payload, the loop is restarted (with variables reset) again from threshold adjustment to indicate that a touch event occurred within a packet transmission.

### C. RX Threshold Control

Alg. 1 shows a conceptual representation of the threshold control algorithm. Similarly to an ED-based CCA, our threshold adjustment is low-complexity, and it does not need to be run continuously. Consequently, it can be activated on demand and run for a limited amount of time to minimize



power consumption. The ED-based threshold control algorithm is based on a linear threshold increase starting from a minimum value  $THR = THR_{min}$  until  $V_{RX}$  is always sampled '0' within a  $T_{min}$  interval. Within  $T_{min}$ , if  $V_{RX}$  is '1', threshold is increased by 1, i.e.,  $THR = THR + 1$ , and the DAC is set to  $THR$ . Once threshold is set and stable so that this condition occurs, the algorithm checks if  $V_{RX}$  is '0' within an additional duration  $T_{timeout}$ . If  $V_{RX}$  is sampled '1' within  $T_{timeout}$ , threshold is increased, timeout counter is reinitialized and a check within  $T_{min}$  is reinforced. If  $V_{RX}$  is sampled '0' within  $T_{timeout}$  the algorithm appends the current threshold to a vector of  $M$  elements  $V_{THR}$ , computes the average threshold  $THR = \overline{V_{THR}}$ , sets the DAC to  $\overline{V_{THR}}$  and exits. In the algorithm we schematized the two counters for  $THR_{min}$  and  $T_{timeout}$  using two independent variables  $t$  and  $\tau$ . To take into account for a setup time or the front-end comparator the algorithm waits for a duration  $\Delta t$ . When the condition  $V_{RX} = '1'$  is triggered the system waits for an additional  $\Delta t_{on}$  hold-off time for the comparator. Voltage  $V_{TH}$  is computed based on the microprocessor supply voltage  $V_{DD}$  and on the used resolution of the DAC, in our case, 8 bit. Observe that provided that threshold is set high enough, it exists a condition so that  $V_{RX}$  is always '0', therefore ensuring that the loop always exits. This condition has been extensively demonstrated through the measurements presented in Sec. VI. This simple algorithm is quite effective even when run during a partial packet reception.

control and event packets that need to be transmitted and received to the BT chip through the PHY interface, in our case a dedicated UART. In this implementation the device can handle a single connection. This is reasonable as the present system is intended to be a personal device, therefore a single client, e.g., a smartphone, needs to be connected at a time. Update BT Status (on the right) parses first any packet from the BT UART port (including events received from the radio front-end) and based on the received packets updates connection status flags. If not connected, the device checks if a connection request has been made and if not, sets the device in advertising mode. Lastly, the BT UART output is parsed again to check if advertising mode has been correctly set by the chip. Observe that the BT chip is fully autonomous w.r.t. the STM32 microprocessor, hence once in advertising mode, the BT chip asynchronously generates UART packets to inform the STM32 of stage changes.

## VI. MEASUREMENTS

### A. Prototype and Proof-of-Concept iOS Application

We have implemented the TX and RX modules shown in Fig. 8, using a standard FR4 dielectric. The RX comprises a copper electrode of size  $5.5\text{ cm} \times 3.6\text{ cm}$ . The TX electrode has a size of  $4\text{ cm} \times 3\text{ cm}$ . To demonstrate the possibility of transmitting push notifications to a more complex and multisensory device that handles elaborated audio and haptic feedback we have implemented a full-custom smartphone application on an Apple® iPhone 8 smartphone running iOS 12. The *Live Wire* agent application once loaded runs in background and provides a text-to-speech output of the content of the payload received through the BCC. The very first time the application is launched a default BCC device needs to be specified (through the CCID automatically generated by the operating system). After this step, the smartphone automatically connects to the specified *Live Wire* RX every time the application is loaded, providing sound alerts in case the RX is out-of-range or the Bluetooth® central manager is turned off. The data transmission from the BCC device to the smartphone is based on a BT notifications mechanism.

### B. Test setup

To verify the correct operation of *Live Wire* and to establish its performance figures, we have designed a specific setup. During the tests, we keep the reference electrode (i.e., the PCB ground plane) of the RX module floating, as in an ordinary operating condition. Grounding the RX would cause a coupling between  $V_{IN}$  and the interference sources of the power supply terminals, therefore impacting on packet error rate. We implemented a  $\mu\text{Py}$  BT streaming routine that transmits both the ADC-sampled output of the front-end, and the main algorithm threshold adjustment phases. At the TX side, we can run both transmission of random packets to establish packet-error rate, or a simple square wave at 550 kHz to establish SNR at the RX input, and consequent signal level at its input.

Fig. 9(a) shows the measurement setup, consisting of a TX plus electrode located on a desk, connected to a PC which provides a BT connection through a dedicated USB Bluegiga

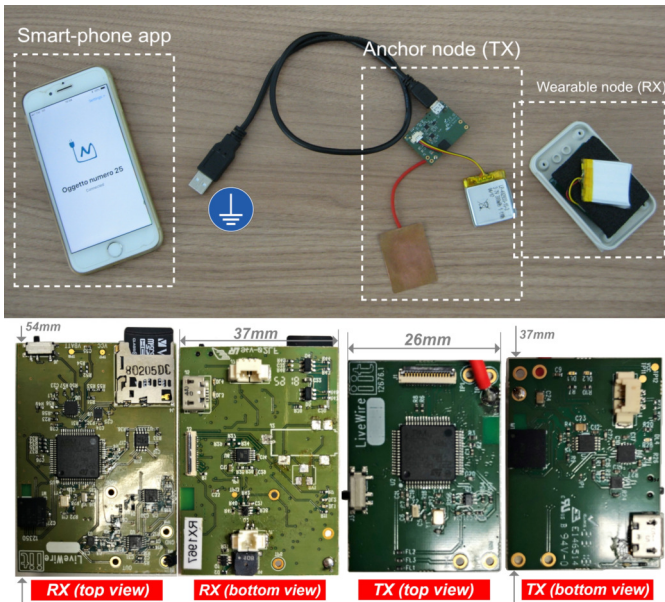


Fig. 8. (top) *Live Wire* prototype (TX and RX) and corresponding iOS phone running an application that receives push notification through BT, and (bottom) photograph of TX and RX PCB with physical size.

### D. Bluetooth® Management

A subset of the commands and events specified in the Bluetooth® BGAPI version 2.6.1 reference manual [41] have been ported in a specific  $\mu\text{Python}$  library implementing packet encapsulation, parsing and decoding of the received event data. The BGAPI library specifies the format of the data,

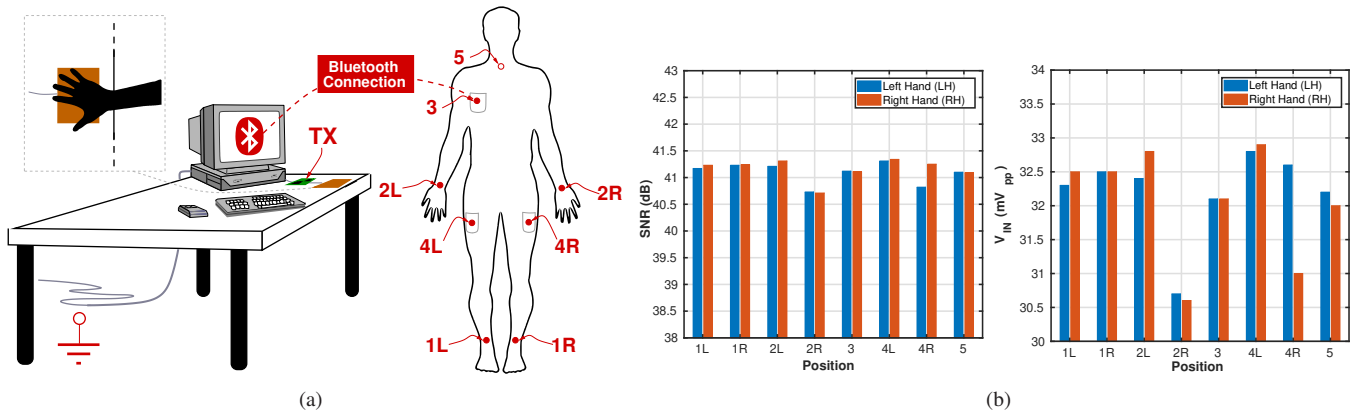


Fig. 9. (a) SNR setup of the input signal when the TX is touched using the left or the right hand (LH, RH) with the RX in different body positions. (b) Measured SNR and input-referred signal level (front-end  $G = 22$ ), 10 MHz input referred noise bandwidth.

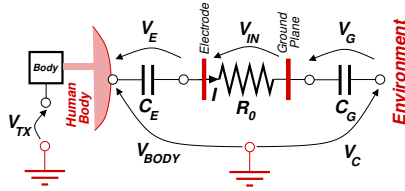


Fig. 10. Simplified lumped model to quantify coupling order of magnitude (quasi-static near-field).

TABLE I

MULTIPLE SUBJECTS SOFT BIOMETRIC DATA

Subject Number	Gender	Age (years)	Height (m)	Weight (kg)
1	Male	25	1.87	82
2	Female	24	1.65	60
3	Male	25	1.83	65
4	Female	18	1.62	57
5	Female	25	1.60	60
6	Female	24	1.62	58
7	Male	24	1.75	68
8	Female	24	1.60	62
9	Male	25	1.80	70
10	Male	25	1.70	71

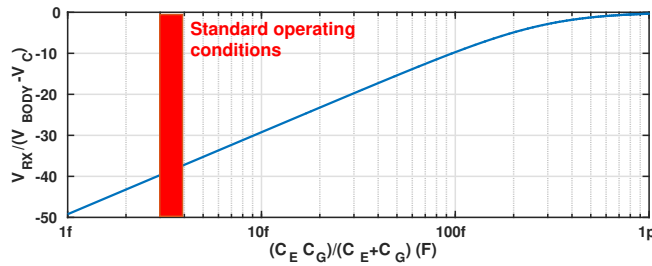


Fig. 11. Signal loss as a function of the series of ground plane and electrode coupling capacitance  $\frac{C_E C_G}{C_E + C_G}$ .

TX electrode using both the left and the right hand (LH, RH, respectively). Based on a measured gain front-end  $G$  of 22 (lower compared to the design due to losses of the PCB components), we have extracted both SNR and equivalent input voltage  $V_{IN}$ . The result is that the SNR is constant throughout the body with a  $\sim 0.5$  dB variation. This effect is given by the low-impedance node to ground provided by construction at the TX.

To understand the order of magnitude of the quantities involved in the transmission, we report the lumped model schematized in Fig. 10. Once the transmitter is touched the  $\sim 3$  V signal that is generated across the electrode terminal is transferred to the human body that emits the signal. We assume that skin-to-electrode contact impedance is in the same order of magnitude of the input impedance of the RX input stage (very high and 1 M $\Omega$  in this implementation). In general, BCC signal propagation can be explained using the several works available in literature to model the human body (in general a network of parallel capacitive and resistive impedance). However, at such low frequency, i.e., 100 kHz–40 MHz, the human body electric field can be considered as quasi-static near-field [4]. Based on our experimental data, at 550 kHz center frequency through the TX, can be received with a 0.83 dB signal loss using an electrode in contact with the skin, referred to the same ground of the TX. This number is obtained using an oscilloscope probe at 10 M $\Omega$  impedance, therefore detecting voltages of  $\sim 3$  V (i.e., the measured voltage, referred to ground on the human body), resulting in peak currents of 300 nA, for a total power dissipation of 30 nW on the human

BT 4.0 dongle. We ran measurements on a single subject and we confirmed SNR findings over subsequent multiple subjects. For the former, the RX is worn by a male subject, 174 m height, 78 Kg weight, aged 37, in different positions (the RX is fixed using an elastic band and the electrode, facing the skin, is not in contact with the skin but with the garment) according to the sketch [for position 3 in Fig. 9(b), the RX is worn in subject's shirt pocket]. For the latter multiple subject measurements, overall ten people was involved. Their soft biometric data shown in Tab. I. Data is acquired using a Python utility program running on the PC, and then elaborated using Matlab®.

### C. Live Wire Signal Level

Fig. 9(b) shows the measured SNR and signal level  $V_{IN}$  obtained using the TX in Continuous Wave (CW) mode (550 kHz square wave), in different locations on the body, namely 1L, 1R, 2L, 3, 2R, 4L, 4R, and 5, by touching the

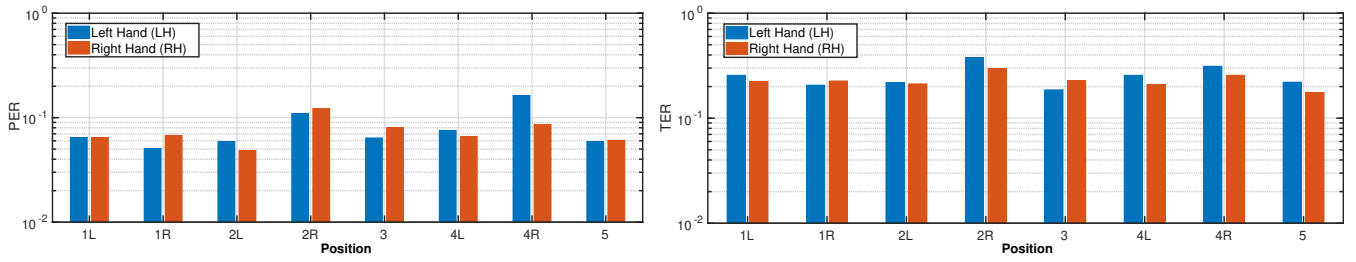


Fig. 12. Packet and Total Error Rate as a function of the positions of the RX on the human body given in Fig. 9(a).

683 body in this condition. This value is well below the safety  
 684 limits stated in [42], that are considered by state-of-the-art  
 685 works [4].

686 We can collapse the core transmission parameters in two  
 687 equivalent capacitive contributions between the two electrodes.  
 688 In turn the RX that is worn on the body can capture the  
 689 radiated signal, thanks to the coupling between the electrode  
 690 terminal to the body and the environment (ground). The  
 691 coupling, in absence of contact with the electrode is capacitive,  
 692 and the current flow depends on the series of these two  
 693 capacitance contributions  $C_E$  and  $C_G$ , the to-body and to-  
 694 ground coupling capacitance, respectively. The RX has a very  
 695 high input impedance that can be modeled as  $R_0$ . The current  
 696 that flows through the body and ground can be determined  
 697 using the Kirchhoff Voltage and Current law, across and  
 698 through the nodes specified in the schematic of Fig. 10.

699 By neglecting the intermediate calculations, the voltage  
 700 across the input stage of the RX can be expressed as,

$$V_{IN} = (V_{BODY} - V_C) \frac{sR_0C_GC_E}{C_G + C_E} \frac{1}{1 + s \frac{R_0C_GC_E}{C_G + C_E}}, \quad (1)$$

701 where  $V_{BODY}$  is the ground referred voltage across the human  
 702 body,  $V_C$ , normally zero, is used to model shunt effect. Observe  
 703 that the RX system is non-coherent, therefore the RX electrode  
 704 positioning can be flipped, i.e., the PCB ground plane can  
 705 face the body while the electrode can face the environment.  
 706 In presence of standard operating conditions  $V_C \sim 0$ , while  
 707 in presence of the shunt effects, experimentally determined  
 708 in Sec. VI-F (that is both PCB plane and electrode are both  
 709 coupled to the body, only),  $V_{BODY} - V_C \sim 0$ , i.e.,  $V_{BODY} \sim V_C$ .

710 Fig. 11 shows a plot of Eqn. (1) as a function of the  
 711 series capacitance  $\frac{C_EC_G}{C_E + C_G}$ . Using the test setup depicted in  
 712 Fig. 9(a)(left), as the input voltage across the RX input stage  
 713 is about  $\sim 33$  mV, we can extract an approximate value of  
 714 the series capacitance that leads to correct device operation,  
 715 in absence of body shunt, which is between 3 fF and 4 fF.  
 716 Observe that the smallest contribution is given by the  $C_G$  which  
 717 needs to be undoubtedly lower compared to  $C_E$ , as the body-  
 718 to-RX separation is times lower compared to PCB-plane to  
 719 ground separation. The current that flows in the RX during a  
 720 pulse transmission is then  $\sim 33$  nA. Observe that the given cou-  
 721 pling capacitance range is consistent with the measurements  
 722 depicted in [15], in which the backwards capacitance falls to  
 723  $\sim 100$  fF for backwards path lengths of 30 cm. In this case, the  
 724 backwards return path is substantially more, therefore leading  
 725 to a very low coupling. The obtained loss, i.e.,  $\sim 19.3$  dB is

726 comparable to the Single-Ended TX–Single-Ended RX case  
 727 shown in [8], with the difference that the TX in our case has  
 728 a low-impedance path to ground. In [8], path loss is about  
 729  $\sim 8$  dB higher [see Fig. 7(c)], due to the TX coupling to ground  
 730 through a capacitor rather than an equivalent resistor. Observe  
 731 that in case an RX electrode is in contact with the skin, one  
 732 between  $C_E$  or  $C_G$  would tend to  $\infty$ , therefore relying on the  
 733 other capacitor coupling to ground.

#### D. Packet Error Rate

734 Fig. 12 shows the measured Packet Error Rate (PER) and  
 735 Total Error Rate (TER) as a function of the positioning of the  
 736 RX. Errors occur because channel injects noise and interfer-  
 737 ence at the receiver input. The number of packet transmitted  
 738 per test is  $N_{TX} = 500$ . The transmitted packets comprises two  
 739 random digits (0–9), and three digits comprising a zero-padded  
 740 progressive packet number, ASCII encoded (one byte per  
 741 digit). The transmitter sends a new packet every 250 ms. We  
 742 define PER, as  $N_{CRC}/N_{RX}$ , and TER, as  $N_{RX}/N_{TX}$ , where  
 743  $N_{CRC}$  are packets with CRC errors,  $N_{RX}$  is the number of  
 744 packets correctly received out of  $N_{TX}$ . Compared to PER, TER  
 745 includes also a measure of missed packet synchronization.  
 746 In this test, the RX is worn in the different body positions  
 747 previously specified, the person stands and touches the TX in  
 748 using both Left or Right Hand (LH and RH, respectively) for  
 749 the complete transmission of the packets. Every time the RX  
 750 detects a packet, it transmits the payload through the BT to  
 751 the PC that associates a time-stamp. This way, we can post-  
 752 process the received data and obtain all the error-rate figures  
 753 of merit.

754 PER and TER are almost independent from the RX posi-  
 755 tioning on the human body leading to an average of  $\sim 0.1$ ,  
 756  $\sim 0.25$ , respectively. The minimum achievable PER depends  
 757 on software implementation. In our  $\mu$ Python solution we have  
 758 kept the garbage collector enabled. Every 1/4 second,  $\mu$ Py  
 759 starts its garbage collection process that has the highest priority  
 760 among any other scheduled task, therefore leading to potential  
 761 synchronization errors. By deactivating the garbage collector  
 762 (even at firmware build time) performance can increase, there-  
 763 fore enabling even lower error-rates.  
 764

#### E. Threshold Control

765 Fig. 13(a) shows a transient plot of the threshold control  
 766 loop operating when the RX is worn in position 3, without  
 767 touching the TX (null input signal). In rest state the algorithm  
 768



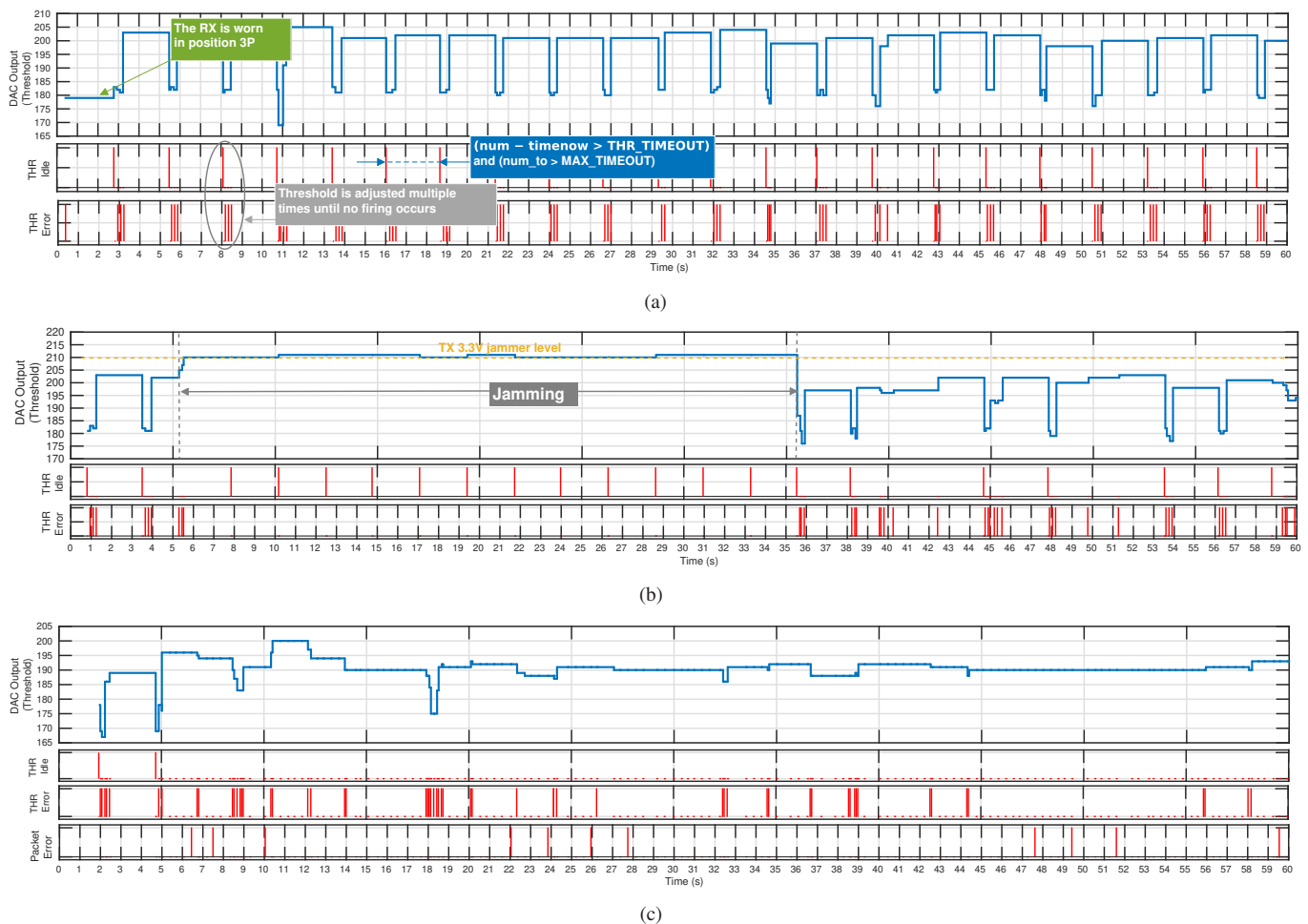


Fig. 13. Threshold adjustment cycles, (a) for configuration 3 given in Fig. 9(a) and 60 s operation without TX packets reception (no input), (b) with multiple jamming, i.e., when the subject repeatedly touches an electrode that generates a fixed 3.3 V square wave at 550 kHz frequency, (c) during a packet error ratio test, in position 5 (LH), with detail on threshold set events and packet error occurrences. Each depicted value represents the final output of Adjust\_THR.

cycles between THR Errors and THR Timeout event adjustments, continuously setting an average threshold of  $\sim 190$ , that corresponds to 2.1 V. This simple test demonstrates that the algorithm converges as the initial threshold set condition is always fixed, and in presence of noise there is always an “escape” condition that leads Adjust\_THR to timeout.

Fig. 13(b) shows a transient plot of the threshold control loop when the subject multiply touches a copper electrode on which a 550 kHz square wave signal at 3.3 V is driven (“Jamming” indication). Once the receiver is jammed, the control loop maintains a high threshold output because the output of the front-end saturates. The THR Idle condition is continuously checked every time the timeout counter is triggered. As soon as the jamming ends, the system restores the previous threshold levels, through another threshold adjustment (lasting a timeout interval). This simple measurement results demonstrate that the control loop returns even in presence of continuous wave interference.

Threshold adjustment is demonstrated to be effective also in presence of a continuous packet transmission from the TX. Fig. 13(c) shows the evolution of the threshold set during a packet error-rate test in position 5. In these conditions, the algorithm successfully tracks the correct DAC level to

maintain a steady threshold of  $\sim 190$ , disregarding packet errors.

To better collocate the threshold set obtained during the error-rate test, by post-processing the received data through the BT link, we have extracted the distribution of the threshold sets over the multiple times the RX runs Adjust\_THR. Fig. 14 shows a histogram (ten bins each) of the threshold set for the correctly received packets only. From the results, it is straightforward that the threshold set strongly depends on the positioning of the device on the human body that captures external interference (that in any case varies over time).

To validate threshold control in presence of interference, we have connected an Agilent 33522A signal generator to the TX electrode and generated a continuous square wave. In this condition a packet error rate test is run. We observed that the result of the test strongly depends on the posture of the subject as well as its relative positioning with respect to the TX (see next subsection for further experiments and details). For instance, when the subject is standing tall, in position 3 [see Fig. 9(a)], a PER of 0.15 (TER of 0.352, average threshold 194) is obtained while injecting a  $1V_{pp}$  signal on the TX electrode at 500 kHz center frequency. To enhance the interference impact we have repeated the tests when the



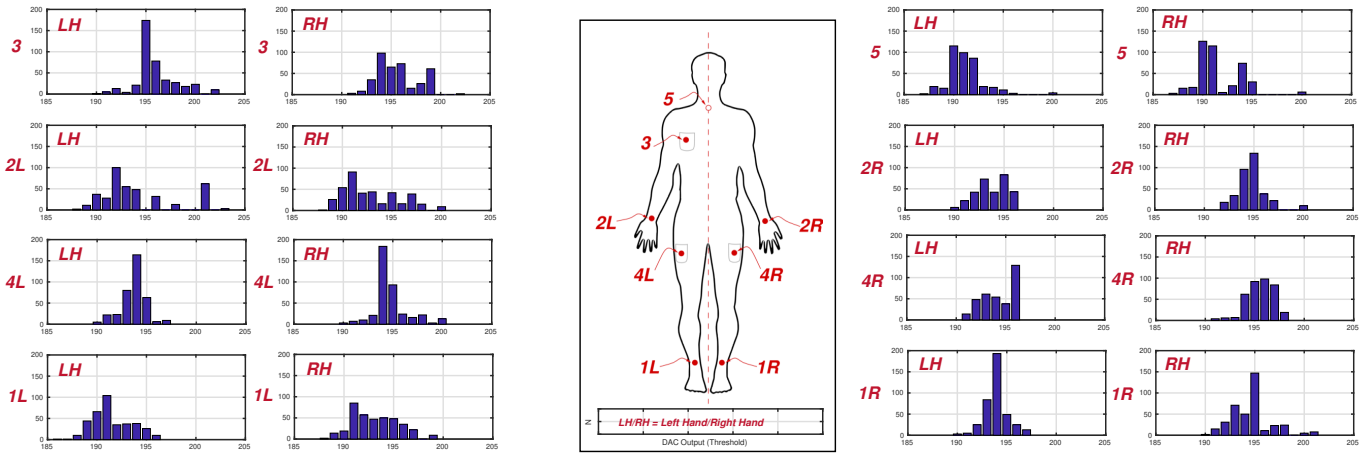


Fig. 14. Histogram of the threshold set corresponding to a correct packet reception as a function of the RX positioning, left and right hand touch (LH, RH). Axes units are specified below the body silhouette.

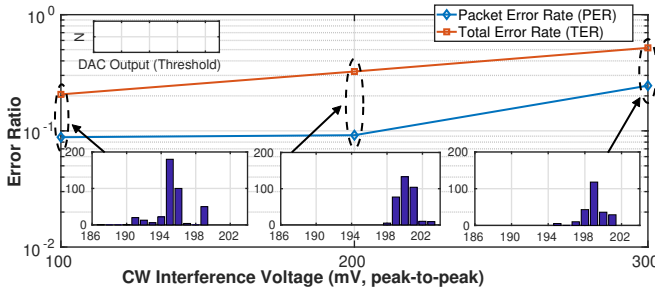


Fig. 15. Impact of CW interference on the performance of the system for different amplitudes, with threshold sets during the experiment corresponding to a correct reception.

subject is sitting on an anti-static chair in front of the desktop shown in Fig. 9(a), using exactly the same signal frequency of 550 kHz, same position 3, and touching the TX using the left hand. Fig. 15 shows the PER and TER degradation as a function of interference amplitude. At 300 mV amplitude the error-rates increase by a factor two. Observe that the threshold set for the three cases progressively increases as the CW interference contributes as an offset across  $V_{RX}$ . These tests demonstrate that the threshold control algorithm successfully counterbalances external disturbances even in presence of strong in-band interference.

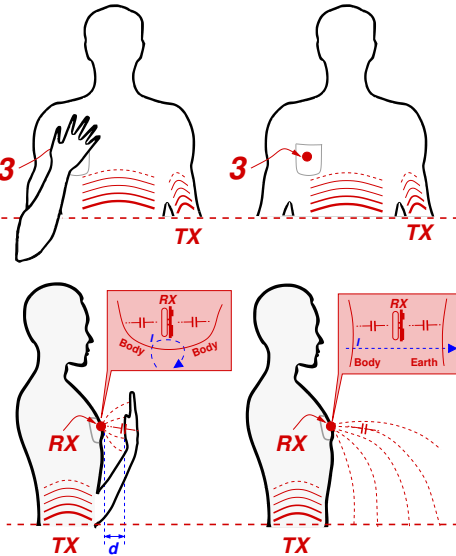
To quantify the Signal-to-Interference Ratio (SIR) corresponding to each injected amplitude level we can compute the average power on the  $1\text{ M}\Omega$  load RX input, starting from the diagram of Fig. 3. By assuming packetizing, i.e., a transmitted number of bits  $N_{\text{bit}}$  (uniformly distributed), for an average duration of  $\bar{T}_s = \frac{T_{s0} + T_{s1}}{2}$ , and packet repetition  $T_r$ , SIR, defined as  $P_{TX}/P_I$  can be written as,

$$SIR = \frac{N_{\text{bit}} \bar{T}_s}{N_{\text{bit}} \bar{T}_s + T_r} \frac{V_{DD}^2}{2V_I^2} (N_w T_p / T_{s0} + 2N_w T_p / T_{s1}). \quad (2)$$

During our test,  $N_{\text{bit}} = 48$  (including triple modular redundancy),  $\bar{T}_s = 909\ \mu\text{s}$ ,  $T_p = \frac{1}{550\text{kHz}}$ ,  $V_{DD} = 2.83\text{ V}$ . By using Eqn. (2), SIR is -3.9 dB for 1 V interference amplitude, and 40.7, 10.2 and 4.5 dB for 100, 200 and 300 mV<sub>pp</sub>, respectively.

### F. Body Shunt

Assuming same distance w.r.t. the skin, the to-ground RX coupling can significantly vary based on the body masking of the return path. Fig. 16(top) exemplifies the concept, we identify as “body shunt”. When the RX is positioned in the subject pocket, the to-ground capacitance can be decreased by shielding the PCB ground plane using a hand. The received signal level is then a function of the spacing between the hand and the RX. Fig. 16(bottom) shows SNR measurement results as a function of the distance of the experimenter right hand w.r.t. the *Live Wire* RX. The shunt effect is not relevant for distance  $d$  greater than 10 cm, while it significantly degrades SNR as the hand gets closer to the device. Based on extensive



$d$ (cm)	SNR (dB)	$V_{IN}$ (mV <sub>pp</sub> )
0 – Complete Cover	6.74	0.6
2	26.54	6.0
5	38.27	23.1
10	39.13	25.5

Fig. 16. (top) Conceptual body shunt sketch. The human body, that is driven by the TX terminal “obscures” the RX, by shunting its terminals, and (bottom) measured SNR as a function of hand-to-device separation  $d$ .

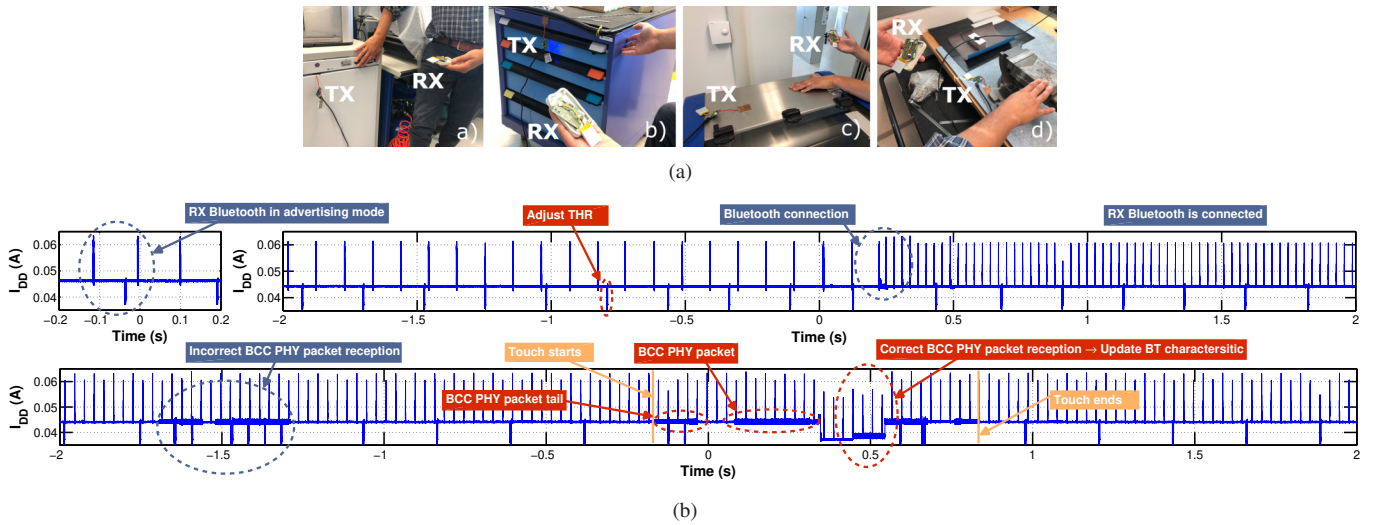


Fig. 17. (a) Different test conditions of the BCC system, with the TX connected through available USB ports in a laboratory environment. In all these conditions, the packets depicted in Fig. 3, are correctly received (no CRC error) from the RX device in the hand of the corresponding author. (b) Example measured RX current through the battery terminals during operation (no buzzer and no audio wave play).

experiments, we have understood that this shunt phenomena can severely decrease signal level, while people garment (e.g., shirts, jackets, sweaters) does not impact significantly on signal level degradation. We conclude that the positioning of the RX device shall account for this degradation and it needs to be worn so that this effect is minimized during its normal use. Alternatively, the front-end gain can be significantly increased to detect lower input voltages  $V_{IN}$  without compromising the required touch-only responsiveness, in any case.

### G. Functional Tests

Fig. 17(a) shows a collection of four test conditions in a laboratory environment for a successful transmission. The TX is installed using the available USB port of nearby PC, and the correct operation of the RX is confirmed by an acoustic signal every time a correct payload is received. In turn the RX is connected through BT (in 4.2 mode, hence, with a payload larger than 20 byte) to the smartphone that provides push text-to-speech notifications once an object is touched. The TX firmware runs a continuous packet transmission containing an ASCII payload *Object X*, where *X* is a letter. In turn this string is transmitted to the smartphone. The TX is connected, respectively, to a) a fridge, b) mechanical drawers, c) a milling machine and d) an iron clamp. The host PC was offline, as the BCC link requires only a ground connection. We observe that in these experiments some spurious packet reception is possible only with proximity, hence, transmission efficiency is a function of the object conductive surface. In first approximation, the bigger the object, the lower the peak-to-peak voltage required at the TX, and in general, the better. Amplitude control can be implemented by limiting the logic swing of the TX output, using, e.g., an adjustable voltage divider that can be configured once, i.e., when the TX is installed in the furniture that is static.

Fig. 17(b) shows the current consumed by the RX through the battery terminals  $I_{DD}$  in an example standard operation

(BT disconnected, BT connected, and during the reception of a PHY packet). The current diagram clearly shows each transition between system states. The average current consumption is 44 mA, resulting in a power consumption of 176 mW (with a measured 4.0 V battery voltage). The TX consumes 100 mW for the transmission shown in Fig. 3. Based on our extensive tests, as expected we have not observed any impact of battery power supply on the performance of the system.

### H. Tests on Multiple Subjects

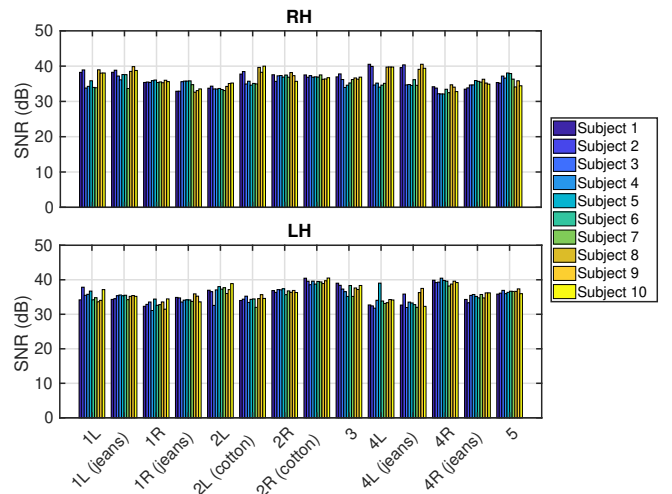


Fig. 18. SNR test on multiple subjects as a function of the RX positioning, left and right hand touch (LH, RH).

We have run tests to verify the correct operation of the device for ten subjects. The tests aimed at establishing both the impact of different bodies and garment on the SNR and verify that the tests on a single subject are confirmed, using the same RX positioning given in Fig. 9(a). Fig. 18 shows the obtained SNR results on the subjects given in

TABLE II  
COMPARISON W.R.T. THE STATE-OF-THE-ART

	This Work	[4]	[1]	[43]
<b>TX Mode</b>	Simplex	Full Duplex	Simplex	Full Duplex
<b>TX Electrode</b>	Any	Confined	Confined	Confined
<b>Electrode Size</b>	5.5 × 3.6 cm (RX)	5 × 5 cm (bowl)	∅ = 0.4 cm	3 × 3 cm <sup>2</sup>
<b>RX to Skin Separation</b>	≤ 2 cm <sup>*</sup>	Contact/Non-Contact <sup>○</sup>	Contact <sup>○</sup>	Contact <sup>○</sup>
<b>Type</b>	Capacitive	Capacitive	Galvanic	Capacitive
<b>Bit rate</b>	1 kbps <sup>*</sup>	21.875 kbps	4.8 kbps	1 kbps
<b>Power Supply</b>	3.7 V Li-Po Battery (RX), 5 V (USB), 3.7 V Li-Po Backup (TX)	7.4 V Battery (mobile), 12 V 480 W switching PSU (fixed nodes)	N/A	3.7 V Li-Po Battery (TX) N/A (RX)
<b>TX Output Power (max)</b>	850 nW	< 4.95 mW <sup>‡</sup>	1 mW <sup>†</sup>	900 nW
<b>TX Output Voltage/Current</b>	2.83 V	5.9 V (min), 9.9 V (max)	± 1 mA on 1 kΩ	10 V
<b>Power Consumption</b>	RX: 176 mW <sup>◊</sup> (including BT) TX: 100 mW <sup>◊</sup>	N/A	RX: 400 mW TX: 16.5 mW	RX: 525 mW TX (token): 148 mW
<b>Error Rate</b>	~0.1 PER, ~0.25 TER	~0.106 PER (best, 1430 bps)	< 10 <sup>-4</sup> BER (35 cm)	< 0.01 BER

N/A = Not Available. N.a. = Not Applicable. ◊ = Calculated based on the measured 44 mA on a 4.0 V (full charge) battery voltage. \* = Limited by the current software implementation. • = Estimated during normal operation, but dependent on capacitive coupling to ground (signal level proportional to  $\frac{C_E C_G}{C_E + C_G}$ ). ○ = Electrodes on skin with or without direct metal contact, i.e., also when covered by a protective plastics. † = Extracted from TX output current. ‡ = Extracted from the paper (9.9 V and < 0.5 mA). ‡ = During protection against remote monitoring tests.

900 Tab. I. During the experiments, the RX electrode is positioned  
901 both directly on the subject skin and on the garment, that  
902 could be jeans and cotton depending on the specific part of  
903 the body. Results shows that garment does not significantly  
904 impact on link performance, as the most impacting factor  
905 is represented by the RX system distance w.r.t. the body  
906 surface. The results do not show a significant variation in the  
907 SNR measurement, for a maximum of 8.4 and 9.4 dB in all  
908 conditions for RH and LH, respectively. This variability can be  
909 attributed to the coupling with the room ground that can vary,  
910 even dynamically, between one test and another. However, this  
911 ground coupling variation does not significantly impact on  
912 system performance as the threshold control can adaptively  
913 adjust the comparator level, although with a cycle of delay  
914 [assuming a worst case step variation of the conditions, 4 s  
915 in the current implementation, see, e.g., Fig. 13(a)]. Once  
916 the threshold control loop runs under these lower signal level  
917 conditions (and adjusts threshold accordingly), the baseband  
918 signal can be still correctly detected. Further measurements in  
919 fact, not shown here for the sake of brevity, confirm the TER  
920 results obtained for a single subject.

921 *I. Comparison with the State-of-the-Art and Discussion*

922 Tab. II shows a performance comparison of *Live Wire* with  
923 respect to the other systems reported in literature. To be  
924 consistent, we have included only the most relevant discrete  
925 components-based systems, rather than integrated solutions,  
926 tightly optimized and achieving extremely low power con-  
927 sumption. Thanks to its inherent low complexity *Live Wire*  
928 well suits aggressively optimized integrated circuit implemen-  
929 tation: in [7], indeed, a simple envelope detector front-end  
930 integrated operating with OOK, 50 kHz center frequency, in  
931 a 65 nm technology provides a ~700 pW simulated power  
932 consumption. However, besides the front-end part of the re-  
933 ceiver, wireless connectivity dominates the power consumption  
934 metric, especially due to the requirement of using standard  
935 connectivity through portable devices that commonly include  
936 BT and Wi-Fi transceivers, rather than ultra-low power solu-  
937 tions such as IR-UWB (here used for ultra-low-power com-

munication rather than localization) [44] that still, are not  
integrated in commercial portable devices.

Thanks to the low-impedance path to ground of the TX  
enforced by construction, and the consequent high SNR  
achievable throughout the body, the system well suits reduced  
supply voltage (2.83 V v.s. the 5.9 V in [4]). More importantly,  
the TX can be of any shape in the furniture, therefore with no  
size limitation. Compared to [45], the system does not require  
very close electrode-skin distance at the RX, which relaxes  
wearable requirements. Thanks to its high input impedance,  
the RX consumes substantially less compared to [43].

949 VII. CONCLUSIONS

950 The design of a BCC system based on a non-coherent  
951 RX architecture was here reported. The system enables ap-  
952 plications in smart infrastructures with increased flexibility  
953 compared to ordinary solutions. Results show that to adapt  
954 the system usage to diverse objects in the environment, the  
955 TX amplitude can be one-time configured once the system  
956 installed in the furniture. The system is ready for applicability  
957 in experiments with visually impaired people and setups to  
958 assess the cognitive improvements that may result both in  
959 terms of training and in terms of enhanced perception.

960 REFERENCES

[1] M. S. Wegmueller, S. Huclova, J. Froehlich, M. Oberle, N. Felber, N. Kuster, and W. Fichtner, "Galvanic Coupling Enabling Wireless Implant Communications," *IEEE Transactions on Instr. and Meas.*, vol. 58, no. 8, pp. 2618–2625, Aug. 2009.

[2] M. S. Wegmueller, M. Oberle, N. Felber, N. Kuster, and W. Fichtner, "Signal Transmission by Galvanic Coupling Through the Human Body," *IEEE Transactions on Instr. and Meas.*, vol. 59, no. 4, pp. 963–969, Apr. 2010.

[3] A. K. Teshome, B. Kibret, and D. Lai, "A Review of Implant Communication Technology in WBAN : Progresses and Challenges," *IEEE Reviews in Biomedical Engineering*, 2018.

[4] V. Varga, G. Vakulya, A. Sample, and T. R. Gross, "Enabling Interactive Infrastructure with Body Channel Communication," *Interactive, Mobile, Wearable and Ubiquitous Technologies*, vol. 1, no. 4, pp. 169–169:29, Dec. 2017.

[5] —, "Playful Interactions with Body Channel Communication: Conquer it!" in *ACM Symposium on User Interface Software and Technology*, Oct. 2017.



[6] Panasonic Achievements Presented at the Exhibition CEATEC 2016. [Online]. Available: <http://www.ceatec.com/2016/news/en-webmagazine/en-005>

[7] S. Maity, D. Yang, B. Chatterjee, and S. Sen, "A sub-nW Wake-up Receiver for Human Body Communication," in *IEEE Biomedical Circuits and Systems Conf.*, Oct. 2018, pp. 1–4.

[8] S. Maity, D. Das, B. Chatterjee, and S. Sen, "Characterization and Classification of Human Body Channel as a function of Excitation and Termination Modalities," in *Int. Conf. of the IEEE Engineering in Medicine and Biology Society (EMBC)*, Jul. 2018, pp. 3754–3757.

[9] P. Chanana, R. Paul, M. Balakrishnan, and P. Rao, "Assistive Technology Solutions for Aiding Travel of Pedestrians with Visual Impairment," *Journal of Rehabilitation and Assistive Technologies Engineering*, vol. 4, Jan. 2017.

[10] H. Ka and S. Ravishankar, "Smart Signage: Technology Enhancing Indoor Location Awareness for People with Visual Impairments," 2016. [Online]. Available: <http://scholarworks.csun.edu/handle/10211.3/180127>

[11] A. R. Jimnez and F. Seco, "Comparing Decawave and Bespoon UWB Location Systems: Indoor/outdoor Performance Analysis," in *IEEE Int. Conf. on Indoor Positioning and Indoor Navigation (IPIN)*, Oct. 2016, pp. 1–8.

[12] T. Grosse-Puppenthal, S. Herber, R. Wimmer, F. Englert, S. Beck, J. von Wilmsdorff, R. Wichert, and A. Kuijper, "Capacitive Near-Field Communication for Ubiquitous Interaction and Perception," Sep. 2014.

[13] Consumer Electronics industry in 2019: Top 5 Trends. [Online]. Available: <https://www.eletimes.com/consumer-electronics-industry-in-2019-top-5-trends>

[14] M. Crepaldi, G. Zini, A. Maviglia, A. Barcellona, A. Merello, and L. Brayda, "Live Wire: Body Channel Communication as a High Impedance and Frequency-scaled Impulse Radio," in *IEEE Biomedical Circuits and Systems Conf.*, Oct. 2017, pp. 1–4.

[15] J. Zhao, J. Mao, T. Zhou, L. Lai, H. Yang, and B. Zhao, "An Auto Loss Compensation System for Non-contact Capacitive Coupled Body Channel Communication," in *IEEE Int. Symposium on Circuits and Systems*, May 2018, pp. 1–5.

[16] J. Mao, B. Zhao, Y. Lian, and H. Yang, "A Self-adaptive Body Channel Communication Scheme for Backward Path Loss Reduction," in *IEEE Int. Symposium on Circuits and Systems*, May 2016, pp. 2034–2037.

[17] J. Bae and H. Yoo, "The Effects of Electrode Configuration on Body Channel Communication Based on Analysis of Vertical and Horizontal Electric Dipoles," *IEEE Transactions on Microwave Theory and Techniques*, vol. 63, no. 4, pp. 1409–1420, Apr. 2015.

[18] P. Tsai, Y. Chang, S. Hsu, and C. Lee, "An OFDM-based 29.1Mbps 0.22nJ/bit Body Channel Communication Baseband Transceiver," in *VLSI Design, Automation and Test*, Apr. 2015, pp. 1–4.

[19] MicroPython. [Online]. Available: <https://micropython.org/>

[20] M. Khamphroo, N. Kwankeo, K. Kaemarungsi, and K. Fukawa, "MicroPython-based Educational Mobile Robot for Computer Coding Learning," in *Int. Conf. of Information and Communication Technology for Embedded Systems*, May 2017, pp. 1–6.

[21] MicroPython May Be Powering Your Next Embedded Device. [Online]. Available: <https://www.designnews.com/electronics-test/micropython-may-be-powering-your-next-embedded-device/164173310860457>

[22] M. Brambring, "Mobility and Orientation Processes of the Blind," in *Electronic Spatial Sensing for the Blind*, 1985, pp. 493–508.

[23] W. Ugulino and H. Fuks, "Landmark Identification with Wearables for Supporting Spatial Awareness by Blind Persons," in *ACM Int. Joint Conf. on Pervasive and Ubiquitous Computing*, Sept. 2015.

[24] A. K. Ganguli, D. Pushp, and A. Chaudhary, "Electronic Travel Aids ETA for Blind Assistance—A Review," *Int. Journal of Engineering Science and Computing*, vol. 6, no. 3, pp. 2672–2675, Mar. 2016.

[25] G. Kleege, "Visible Braille/Invisible Blindness," *Journal of Visual Culture*, vol. 5, no. 2, pp. 209–218, Aug. 2006.

[26] (2011–2014, Jun.) An1391: Introduction to the bodycom technology. [Online]. Available: [ww1.microchip.com/downloads/en/AppNotes/00001391C.pdf](http://ww1.microchip.com/downloads/en/AppNotes/00001391C.pdf)

[27] P. N. Whatmough, G. Smart, S. Das, Y. Andreopoulos, and D. M. Bull, "A 0.6V All-Digital Body-Coupled Wakeup Transceiver for IoT Applications," in *Symposium on VLSI Circuits (VLSI Circuits)*, Jun. 2015, pp. C98–C99.

[28] J. Jang, H. Cho, and H. Yoo, "An 802.15.6 HBC Standard Compatible Transceiver and 90 pJ/b Full-Duplex Transceiver for Body Channel Communication," in *IEEE Biomedical Circuits and Systems Conf.*, Oct. 2019, pp. 1–4.

[29] Christiane Attig and Nadine Rauh and Thomas Franke and Josef F. Krems, "System Latency Guidelines Then and Now – Is Zero Latency Really Considered Necessary?" in *HCI*, 2017.

[30] J. Huang, L. Wang, D. Zhang, and Y. Zhang, "A Low-frequency Low-noise Transceiver for Human Body Channel Communication," in *IEEE Biomedical Circuits and Systems Conf.*, Nov. 2009, pp. 37–40.

[31] H. Cho, H. Kim, M. Kim, J. Jang, Y. Lee, K. J. Lee, J. Bae, and H. Yoo, "A 79 pJ/b 80 Mb/s Full-Duplex Transceiver and a 42.5μW 100 kb/s Super-Regenerative Transceiver for Body Channel Communication," *IEEE Journal of Solid-State Circuits*, vol. 51, no. 1, pp. 310–317, Jan. 2016.

[32] H. Cho, J. Bae, and H. Yoo, "A 39 μW Body Channel Communication Wake-up Receiver with Injection-locking Ring-oscillator for Wireless Body Area Network," in *IEEE Int. Symposium on Circuits and Systems*, May 2012, pp. 2641–2644.

[33] H. Cho, H. Kim, M. Kim, J. Jang, Y. Lee, K. J. Lee, J. Bae, and H. Yoo, "A 79 pJ/b 80 Mb/s Full-Duplex Transceiver and a 42.5μW 100kb/s Super-Regenerative Transceiver for Body Channel Communication," *IEEE Journal of Solid-State Circuits*, vol. 51, no. 1, pp. 310–317, Jan. 2016.

[34] M. A. Hannan, S. M. Abbas, S. A. Samad, and A. Hussain, "Modulation Techniques for Biomedical Implanted Devices and Their Challenges," *Sensors (Basels)*, vol. 1, no. 12, pp. 297–319, Dec. 2012.

[35] M. Crepaldi and P. Kinget, "Error Ratio Model for Synchronised-OOK IR-UWB Receivers in AWGN Channels," *Electronics Letters*, vol. 49, no. 1, pp. 25–27, Jan. 2013.

[36] S. Vijayalakshmi and V. Nagarajan, "Energy efficient low density parity check scheme for body channel communication using FPGA," *Microprocessors and Microsystems*, vol. 68, pp. 84 – 91, 2019.

[37] J. Hwang, T. Kang, J. Kwon, and S. Park, "Effect of Electromagnetic Interference on Human Body Communication," *IEEE Transactions on Electromagnetic Compatibility*, vol. 59, no. 1, pp. 48–57, Feb. 2017.

[38] X. Ling, B. Wu, H. Wen, P. Ho, Z. Bao, and L. Pan, "Adaptive Threshold Control for Energy Detection Based Spectrum Sensing in Cognitive Radios," *IEEE Wireless Communications Letters*, vol. 1, no. 5, pp. 448–451, Oct. 2012.

[39] MicroPython Documentation – Release 1.9.2. [Online]. Available: <https://media.readthedocs.org/pdf/micropython/latest/micropython.pdf>

[40] Zecheng Xie, Rongtao Xu, and Lei Lei, "A Study of Clear Channel Assessment Performance for Low Power Wide Area Networks," in *Int. Conf. on Wireless Communications, Networking and Mobile Computing*, Sep. 2014, pp. 311–315.

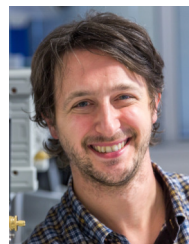
[41] Bluetooth Smart Software API Reference Manual. [Online]. Available: <https://www.silabs.com/documents/login/reference-manuals/bluetooth-api-reference-261.pdf>

[42] "Guidelines for Limiting Exposure to Time-Varying Electric, Magnetic, and Electromagnetic Fields (up to 300 GHz)," in *Health Physics*, 1998, pp. 494–522.

[43] V. Nguyen, M. Ibrahim, H. Truong, P. Nguyen, M. Gruteser, R. Howard, and T. Vu, "Body-Guided Communications: A Low-power, Highly-Confinned Primitive to Track and Secure Every Touch," in *Int. Conf. on Mobile Computing and Networking*, 2018, pp. 353–368.

[44] R. Liu, B. R. Carlton, S. Pellerano, F. Sheikh, D. S. Vemparala, A. Ali, and V. S. Somayazulu, "A 264-μW 802.15.4a-Compliant IR-UWB Transmitter in 22nm FinFET for Wireless Sensor Network Application," in *IEEE Radio Frequency Integrated Circuits Symposium (RFIC)*, Jun. 2018, pp. 164–167.

[45] M. S. Wegmueller, W. Fichtner, M. Oberle, and N. Kuster, "BPSK & QPSK Modulated Data Communication for Biomedical Monitoring Sensor Network," in *IEEE Int. Conf. of the Engineering in Medicine and Biology Society*, Aug. 2006, pp. 2071–2074.



**Marco Crepaldi (M<sup>9</sup>)** received the engineering degree (summa cum laude) and the Ph.D. in electronic engineering from the Politecnico di Torino (Polito), Turin, Italy, in 2005 and 2009, respectively. During 2008 he was a Visiting Scholar at the Electrical Engineering Department of Columbia University in the City of New York. After the Ph.D., he worked as a Postdoc at the VLSI-Lab, Electrical Engineering department, PoliTo, and then as a Postdoc at the former Istituto Italiano di Tecnologia@PoliTo Center for Space Human Robotics (IIT-CSHR). He is now

the coordinator of the Electronics Design Lab (edl.iit.it) at the IIT Center for Human Technology in Genova. His scientific activity is related to the analysis, simulation and development of integrated event-driven and all-digital Impulse-Radio Ultra-Wide Band (IR-UWB) systems. He is author and co-author of more than 60 publications and two international patents.



1132  
1133  
1134  
1135  
1136  
1137  
1138  
1139  
1140  
1141  
1142  
1143  
1144  
1145  
1146



**Alessandro Barcellona** received the engineering degree (summa cum laude) in automation engineering from University of Palermo in 2007. He obtained a research grant in Biophysics field at the National Research Council (CNR) of Palermo for the hardware and software design of the instrumentation electronic control and command for Atomic Force Microscopy (AFM) on living cells. He joined the Nanophysics department of the Istituto Italiano di Tecnologia (IIT) and his main activities regarded the hardware and software design and implementation of electronic devices for open source and automated microscopy imaging systems. He is now a technician of the Electronic Design Lab (edl.iit.it) facility. His main activities regard hardware design, short-term electrical & physical design, reworking and assembly management.

1147  
1148  
1149  
1150  
1151  
1152  
1153  
1154  
1155  
1156  
1157



**Giorgio Zini** received the high school diploma in 1978 (Liceo Scientifico L. Respighi in Piacenza) and developed a deep knowledge in electronic design and R&D management working (since 1979) as employee in several companies (Computer Application Engineering and Silverstar Ltd. in Milan, Ansaldo S.p.A., Esacontrol and Orsi Automazione s.r.l. in Genova, Rubbini s.r.l. in Bologna) and also as a member of a R&D company (LUZ elettronica in Piacenza). He worked as a consultant for prestigious firms and organizations like Siemens S.p.A., DESY Accelerator Consortium, British Petroleum, Enel, Ferrovie Italiane and Università di Genova. Now he is Senior Electronic Designer in Electronic Design Laboratory (EDL) of the Istituto Italiano di Tecnologia (IIT, Genova). His experience covers many fields in electronic engineering: microprocessor and embedded microcontroller systems, analog data acquisition systems, digital signal processors, FPGA and CPLD devices, high speed data transmission in local area and wide area networks, switched mode power supplies, PWM motor controllers, very-low power battery operated and solar-cells powered devices. During his 39 year career Mr. Zini successfully designed (or participated in the development of) hundreds of electronic systems ranging from small pocket devices, to large industrial plants.

1169  
1170  
1171  
1172  
1173  
1174  
1175  
1176  
1177  
1178  
1179  
1180  
1181



**Alberto Ansaldo** holds a MSc in Electronics Engineering and a Ph.D. in Communication Science and Technology focused on chemical vapor deposition of carbon nanotubes for electronic applications. He joined the Italian Institute of Technology in 2008 as a founder of the Soft Materials Design Laboratory, mainly working in carbon nanomaterial composite applications in robotics and neuroprosthetics. In 2015, he joined the IIT Graphene Labs. His current research interests encompass 2D crystals production and applications, with a focus on supercapacitors and Li-ion batteries. He is currently an R&D specialist at ASG Superconductors. He is author of more than 70 publications and 8 granted patents.

1182  
1183  
1184  
1185  
1186  
1187  
1188  
1189  
1190  
1191  
1192  
1193  
1194  
1195  
1196  
1197  
1198  
1199  
1200  
1201  
1202  
1203



**Paolo Motto Ros** is Senior Post-Doc Researcher at Politecnico di Torino (Torino, Italy), Dipartimento di Elettronica e Telecomunicazioni, with the MiNES (Micro&Nano Electronic Systems) group. He received the electronic engineering degree and the Ph.D. in electronic engineering from the Politecnico di Torino, Torino, Italy, in 2005 and 2009, respectively. From 2009 to 2012 he was with Neuronica Laboratory (Dipartimento di Elettronica, Politecnico di Torino) as post-doc researcher, jointly with, 2006-2011, Istituto Nazionale Fisica Nucleare, INFN, Italy. From 2012 to 2019 he was with Istituto Italiano di Tecnologia (Center for Space Human Robotics, CSHR, Torino, Italy, and, since 2016, Electronic Design Laboratory, EDL, Genova, Italy) as senior (since 2014) post-doc researcher. He joined the Politecnico di Torino, Dipartimento di Elettronica e Telecomunicazioni, in 2019. He is an IEEE member since 2016, and member of the Circuits And Systems (CAS) society; he was member of the organizing staff of the IEEE BioCAS 2017 conference, and member of the organizing committee of the IEEE ICECS 2019 conference. He counts >40 publications; current research interests include: event-driven digital integrated circuits, architectures, and systems; low-power smart sensor networks; bio-inspired electronics; biomedical and humanoid robotic applications.



**Alessandro Sanginario** received the masters degree in biomedical engineering and the Ph.D. degree in physics from the Politecnico di Torino, in 2006 and 2011, respectively. From 2006 to 2007, he was with the Chilab Material and Microsystems Laboratory, Politecnico di Torino. He was a Visiting Ph.D. Student with the Vestfold University College, Norway, during his Ph.D. period. From 2012 to 2017, he held a Post-Doctoral position at the Center for Space Human Robotics, with the Italian Institute of Technology. He is now research technician with Electronics Dept. of Politecnico di Torino. His research interests concern microelectromechanical systems and advanced sensors, in particular, for biomedical applications.

1204  
1205  
1206  
1207  
1208  
1209  
1210  
1211  
1212  
1213  
1214  
1215  
1216  
1217



**Claudia Cuccu** received Bachelors degree in Biomedical Engineering at University of Cagliari in 2016 and received Masters degree in Biomedical Engineering with major in Biomedical instrumentation at Politecnico di Torino in October 2019, discussing a thesis entitled: "Modeling and characterization of a body channel communication system". Main research interests are Biomedical Signal Processing, Body channel communication, and Bionanotechnologies.

1218  
1219  
1220  
1221  
1222  
1223  
1224  
1225  
1226  
1227  
1228



**Danilo Demarchi** (M10-SM13) received Engineering Degree and Ph.D. in Electronics Engineering from Politecnico di Torino, Italy, in 1991 and 1995, respectively. Full position as Associate Professor at Politecnico di Torino, Department of Electronics and Telecommunications. Visiting Professor at EPFL Lausanne and at Tel Aviv University. Visiting Scientist (August 2018) at MIT and Harvard Medical School. Author and co-author of 3 patents and more than 200 scientific publications in international journals and peer-reviewed conference proceedings. Leading the MiNES (Micro&Nano Electronic Systems, <http://mines.polito.it>) Laboratory of Politecnico di Torino. Member of the BioCAS Technical Committee, Associate Editor of the Transactions on Biomedical Circuits and Systems (TBioCAS), of the Open Journal of Engineering in Medicine and Biology (OJ-EMB), of IEEE Sensors and of the Springer-Nature Journal BioNanoScience. General Chair of BioCAS 2017 (Biomedical Circuits and Systems) and founder of IEEE FoodCAS Workshop (Circuits and Systems for the Food Chain).

1229  
1230  
1231  
1232  
1233  
1234  
1235  
1236  
1237  
1238  
1239  
1240  
1241  
1242  
1243  
1244  
1245  
1246  
1247



**Luca Brayda** obtained his MSc in Computer Science Engineering at Politecnico di Torino in 2003, with a Master Thesis at the Panasonic Speech Technology lab of Santa Barbara, USA, supervised by Jean-Claude Junqua and Luca Rigazio. In 2007 he got his PhD from the University of Nice-Sophia Antipolis, France, supervised by Christian Wellekens and Maurizio Omologo. His research on microphone arrays for robust speech recognition was hosted by the Eurecom Institute, France and by the Fondazione Bruno Kessler, Trento, Italy. From 2008 he is Team Leader at the Italian Institute of Technology, in the Robotics, Brain and Cognitive Sciences dept., headed by Giulio Sandini. He has worked in multimedia communications, telerobotics and virtual environments. His current interests are on haptics, acoustics and audio augmented reality, with applications in assistive technologies to compensate sensory impairment and augment human capabilities. He was coordinator of the European FP7 STREP 2014-2017 project BLINDPAD ([www.blindpad.eu](http://www.blindpad.eu)). He is author of more than 30 international publications and 2 international patents.

1248  
1249  
1250  
1251  
1252  
1253  
1254  
1255  
1256  
1257  
1258  
1259  
1260  
1261  
1262  
1263  
1264  
1265  
1266

RESPONSES TO REVIEWERS' COMMENTS

AE COMMENTS

The authors have satisfactorily addressed many of the most important issues raised by the reviewers. However, the manuscript still has some deficiencies with respect to language use. Several typos and language problems remain throughout the revised submission. The authors should have the paper carefully proofread and revised before resubmission.

Thank you again for having coordinated the review of our paper and for having brought to us these important points. We have now carefully re-checked the complete manuscript sentence by sentence and adjusted these English mistakes. We have also checked the manuscript for other errors (e.g., figures numbering) and corrected them.

In addition, in the new experimental results with multi-subjects, it is unclear what would be the overall impact of a 9.4dB variability in the overall functionality of the device. The authors are encouraged to include a brief discussion in that regard.

Thanks for the suggestion. We have now briefly discussed this impact on L910-920.

REVIEWER 1

This paper is a revision of an earlier submission and describes a body-channel-communication (BCC) system. My first review raised a number of issues. These issues have been addressed by removing some content, adding an additional evaluator, and enlarging the description of the (low-level) PHY protocol/implementation.

Thank you again for the helpful suggestions. We think that your suggestions helped us improving a lot our manuscript.

One of the strong points of the first version was that it introduced an interesting application scenario. The current version has reduced this part to just briefly mention this problem domain. In the end, this decision of the authors should be applauded, as the evidence to support the use of this BCC implementation to assist visually-impaired person was weak.

Thank you again for the suggestion.

As a result of these changes, the main topic of the paper is the low-level hardware and software of a PHY layer for BCC. This part is difficult to read (see language comments below) and – maybe – of moderate interest to the readers of this journal.

We have now tried to process the manuscript and carefully proof-read it to eliminate English mistakes and correct other reference mistakes we have found (e.g., figure numbering).

Some of the figures are impossible to read without substantial magnification (e.g., Fig 7; only at 400x can the labels be read). Or the figures are confusing (e.g., Fig 13 with different scales on the x-axis of (a), (b), and (c), as well as different ranges for these three sub-figures). Is

there any reason to show these three figures aligned in one figure?

The reason to show these three sub-figures aligned vertically is to optimize space not to increase paper length, and at the same time maintain readability. The different x-axis spans are related directly to the phenomena we wanted to observe, and they are not necessarily equal. However, we have decided to uniform the x-axes for all figures with a 60s span.

Moreover, since it was not readable enough, we have now increased font size of Fig. 6, as well.

In the discussion of Modulation and Signaling,  $N_w$  is introduced as “Each symbol comprises a square wave of  $N_w$  periods”, but it’s shown in Fig. 3 as a time interval. And are these pulses really part of  $T_{s0}$  as Fig. 3 suggests?

Thanks for pointing this out. Indeed the correct indication is  $N_w T_p$  because the indicated label must have time units. We have now corrected the figure and added a note on L279-280 to make clearer.

The x-axis and the y-axis of Fig. 14 have no labels.

Please consider that the x and y-labels in the figure are specified in the center of the figure below the human body silhouette. These labels apply to all axes in the figure. We have modified the caption of the figure to make clearer.

Furthermore, even in its current form, the paper contains many English language issues (e.g., subject verb agreement, wrong word – “variegated environmental objects” [color was never discussed before], “The literature is disseminated with Electronic Travel Aids (ETA)” [maybe populated? filled with? ]).

Thanks for the suggestion. We have now reprocessed to manuscript to improve the English form.

REVIEWER 2

The revised paper R1 addressed most of my comments and suggestions. It reads better now, though with an effort because it was edited in MS Word and it kept a lot of strikethrough text...

Thank you for having reviewed again our paper. We are sorry if the font encoding does not look well but we are using the IEEE tran Latex package, combined with Latexdiff to enlighten text additions and removals. Maybe you are referring to the difference file and not to the full manuscript. We had submitted them both on the TETC site. This was the default font that was implemented in the Latex package. We have decided not to change this not to impact on page length, therefore making it difficult to the reviewers to check if the length of the manuscript exceeds the specifications of the journal.